

---

# MULTI-VIEW DATA VISUALISATION VIA MANIFOLD LEARNING

---

**Theodoulos Rodosthenous\***  
Department of Mathematics  
Imperial College London  
London, SW7 2AZ, UK  
tr1915@ic.ac.uk

**Vahid Shahrezaei**  
Department of Mathematics  
Imperial College London  
London, SW7 2AZ, UK  
v.shahrezaei@imperial.ac.uk

**Marina Evangelou**  
Department of Mathematics  
Imperial College London  
London, SW7 2AZ, UK  
m.evangelou@imperial.ac.uk

February 28, 2025

## ABSTRACT

Non-linear dimensionality reduction can be performed by *manifold learning* approaches, such as Stochastic Neighbour Embedding (SNE), Locally Linear Embedding (LLE) and Isometric Feature Mapping (ISOMAP). These methods aim to produce two or three latent embeddings, primarily to visualise the data in intelligible representations. This manuscript proposes extensions of Student's t-distributed SNE (t-SNE), LLE and ISOMAP, for dimensionality reduction and visualisation of *multi-view* data. Multi-view data refers to multiple types of data generated from the same samples. The proposed multi-view approaches provide more comprehensible projections of the samples compared to the ones obtained by visualising each data-view separately. Commonly visualisation is used for identifying underlying patterns within the samples. By incorporating the obtained low-dimensional embeddings from the multi-view manifold approaches into the  $K$ -means clustering algorithm, it is shown that clusters of the samples are accurately identified. Through the analysis of real and synthetic data the proposed *multi-SNE* approach is found to have the best performance. We further illustrate the applicability of the multi-SNE approach for the analysis of multi-omics single-cell data, where the aim is to visualise and identify cell heterogeneity and cell types in biological tissues relevant to health and disease.

**Keywords** Multi-view Data · Data Visualisation · Manifold Learning · Clustering

## 1 Introduction

Data visualisation is an important and useful component of exploratory data analysis, as it can reveal interesting patterns in the data and potential clusters of the observations. A common approach for visualising high-dimensional data ( $p \gg n$ ) is by reducing its dimensions. Linear dimensionality reduction methods, including Principal Components Analysis (PCA) [Jolliffe and Cadima, 2016] and Non-negative Matrix Factorization (NMF) [García et al., 2018], assume linearity within data sets and as a result these methods often fail to produce reliable representations when linearity does not hold. *Manifold learning*, an active research area within machine learning, in contrast to the linear dimensionality reduction approaches do not rely on any linearity assumptions. By assuming that the dimensions of the data sets are artificially high, manifold learning methods aim to capture important information in an induced low-dimensional embedding [Zheng and Xue, 2009]. The generated low-dimensional embeddings can be used for data visualisation in the 2-D or 3-D spaces.

Manifold learning approaches used for dimensionality reduction and visualisation, focus on preserving at least one of the characteristics of the data. For example, the Stochastic Neighbour Embedding (SNE) preserves the probability distribution of the data [Hinton and Roweis, 2003]. The Locally Linear Embedding (LLE) proposed by Roweis and Saul [2000] is a neighbourhood-preserving method. The Isometric Feature Mapping (ISOMAP) proposed by Tenenbaum et al. [2000] is a quasi-isometric method based on Multi-Dimensional Scaling [Kruskal, 1964]. Spectral Embedding finds low-dimensional embeddings via spectral decomposition of the Laplacian matrix [Ng et al., 2001]. The Local

---

\*Contact author

Tangent Space Alignment method proposed by Zhang and Zha [2004] learns the embedding by optimising local tangent spaces representing the local geometry of each neighbourhood and Uniform Manifold Approximation and Projection preserves the global structure of the data by constructing a theoretical framework based in Riemannian geometry and algebraic topology [McInnes et al., 2018].

This manuscript focuses on data visualisation of *multi-view data*, which are regarded as different types of data sets that are generated on the same samples of a study. It is very common nowadays in many different fields to generate multiple data-views on the same samples. For example, multi-view imaging data describe distinct visual features such as local binary patterns (LBP), and histogram of oriented gradients (HOG) [Shen et al., 2013], while multi-omics data, *e.g. proteomics, genomics, etc.*, in biomedical studies quantify different aspects of an organism’s biological processes [Hasin et al., 2017]. Through the collection of multi-view data, researchers are interested in better understanding the collected samples, including their visualisation, clustering and classification. Analysing simultaneously the multi-view data is not a straightforward task as each data-view has its own distribution and variation pattern [Rodosthenous et al., 2020].

Several approaches have been proposed for the analysis of multi-view data. These include methods on clustering [Kumar et al., 2011, Liu et al., 2013, Sun et al., 2015, Ou et al., 2016, Ye et al., 2018, Ou et al., 2018, Wang et al., 2021], classification [Shu et al., 2019], regression [Li et al., 2019], integration [Rodosthenous et al., 2020] and dimensionality reduction [Sun, 2013, Zhao et al., 2018, Xu et al., 2015]. Such approaches have been extensively discussed in the review papers of Xu et al. [2013] and Zhao et al. [2017].

In this manuscript, we focus on the visualisation task. By visualising multi-view data the aim is to obtain a global overview of the data and identify patterns that would have potentially be missed by looking at each data-view separately. Typically, multiple visualisations are produced, one from each data-view, or the features of the data-views are concatenated to produce a single visualisation. The former could provide misleading outcomes, with each data-view revealing different visualisations and patterns. The different statistical properties, physical interpretation, noise and heterogeneity between data-views suggest that concatenating features would often fail in achieving a reliable interpretation and visualisation of the data [Fu et al., 2008].

Multi-view visualisation has been explored in the literature by Xie et al. [2011] and Shen et al. [2013], proposing extensions of the manifold approaches t-SNE and LLE, named m-SNE and m-LLE, respectively. M-SNE combines the probability distributions produced by each data-view into a single distribution via a weight parameter. It then implements the solution by applying t-SNE on the combined distribution to obtain a single low-dimensional embedding. The algorithm finds the optimal choice for both the low-dimensional embeddings and the weight parameter simultaneously. Multi-view Locally Linear Embeddings (m-LLE) is an extension of LLE and it was primarily developed to effectively retrieve medical images [Shen et al., 2013]. M-LLE produces a single low-dimensional embedding by integrating the embeddings from each data-view according to a weight parameter  $c$ , which refers to the contribution of each data-view. Similarly to m-SNE, the algorithm optimizes both the weight parameter and the embeddings simultaneously.

Building on from the existing literature work, we propose here alternative extensions to the manifold approaches: t-SNE, LLE, and ISOMAP, for visualising multi-view data. The cost functions of our proposals are different from the existing ones, as they integrate the available information from the multi-view data iteratively. At each iteration, the proposed *multi-SNE* updates the low-dimensional embeddings by minimising the dissimilarity between their probability distribution and the distribution of each data-view. The total cost of this approach equals to the weighted sum of those dissimilarities. Our proposed variation of LLE, *Multi-LLE*, constructs the low-dimensional embeddings by utilising a consensus weight matrix, which is taken as the weighted sum of the weight matrices computed by each data-view. Lastly, the low-dimensional embeddings in the proposed *multi-ISOMAP* are constructed by using a consensus graph, for which the nodes represent the samples and the edge lengths are taken as the averaged distance between the samples in each data-view.

Through a comparative study via the analysis of real and synthetic data we illustrate that our proposals result to more robust solutions compared to both m-SNE and m-LLE. We further illustrate through the visualisation of the low-dimensional embeddings produced by the proposed multi-view manifold learning algorithms, that if clusters exist within the samples, they can be successfully identified. We show that this can be achieved by applying the  $K$ -means algorithm on the low-dimensional embeddings of the data. The  $K$ -means [MacQueen, 1967] was chosen to cluster the data points, as it is one of the most famous and prominent partition clustering algorithms [Xu et al., 2015]. A better clustering performance by  $K$ -means suggests a visually clearer separation of clusters. Through the conducted experiments, we show that the proposed multi-SNE approach recovers well-separated clusters of the data, and has comparable performance to multi-view clustering algorithms that exist in the literature.

## 2 Material and Methods

In this section, the proposed approaches for multi-view manifold learning are described. This section starts with an introduction of the notation used throughout this manuscript. The proposed multi-SNE, multi-LLE and multi-ISOMAP are described in Sections 2.2, 2.3 and 2.4, respectively. The section ends with a description of the process for tuning the parameters of the algorithms.

### 2.1 Notation

Throughout this paper, the following notation is used:

- $N$ : The number of samples.
- $X \in \mathbb{R}^{N \times p}$ : A single-view data matrix, representing the original high-dimensional data used as input;  $\mathbf{x}_i \in \mathbb{R}^p$  is the  $i^{\text{th}}$  data point of  $X$ .
- $M$ : The number of data-views in a given data set;  $m \in \{1, \dots, M\}$  represents an arbitrary data-view.
- $X^{(m)} \in \mathbb{R}^{N \times p_m}$ : The  $m^{\text{th}}$  data-view of multi-view data;  $\mathbf{x}_i^m \in \mathbb{R}^{p_m}$  is the  $i^{\text{th}}$  data point of  $X^{(m)}$ .
- $Y \in \mathbb{R}^{N \times d}$ : A low-dimensional embedding of the original data.  $\mathbf{y}_i \in \mathbb{R}^d$  represents the  $i^{\text{th}}$  data point of  $Y$ . In this manuscript,  $d = 2$ , as the focus of the manuscript is on data visualisation.

### 2.2 Multi-SNE

SNE, proposed by Hinton and Roweis [2003], measures the probability distribution,  $P$  of each data point  $\mathbf{x}_i$  by looking at the similarities among its neighbours. For every sample  $i$  in the data,  $j$  is taken as its potential neighbour with probability  $p_{ij}$ , given by

$$p_{ij} = \frac{\exp(-d_{ij}^2)}{\sum_{k \neq i} \exp(-d_{ik}^2)},$$

where  $d_{ij} = \frac{\|\mathbf{x}_i - \mathbf{x}_j\|^2}{2\sigma_i^2}$  represents the dissimilarity between points  $\mathbf{x}_i$  and  $\mathbf{x}_j$ . The value of  $\sigma_i$  is either set by hand or found by binary search [van der Maaten and Hinton, 2008]. Based on this value, a probability distribution of sample  $i$ ,  $P_i = \sum_j p_{ij}$ , with fixed perplexity is produced. Perplexity refers to the effective number of local neighbours and it is defined as  $Perp(P_i) = 2^{H(P_i)}$ , where  $H(P_i) = -\sum_j p_{ij} \log_2 p_{ij}$  is the Shannon entropy of  $P_i$ . It increases monotonically with the variance  $\sigma_i$  and typically takes values between 5 and 50.

In the same way, a probability distribution in the low-dimensional space,  $Y$ , is computed as follows:

$$q_{ij} = \frac{\exp(-\|\mathbf{y}_i - \mathbf{y}_j\|^2)}{\sum_{k \neq i} \exp(-\|\mathbf{y}_i - \mathbf{y}_k\|^2)},$$

which represents the probability of point  $i$  selecting point  $j$  as its neighbour.

The induced embedding output,  $\mathbf{y}_i$ , represented by probability distribution,  $Q$ , is obtained by minimising the Kullback-Leibler divergence (KL-divergence)  $KL(P||Q)$  between the two distributions  $P$  and  $Q$  [Kullback and Leibler, 1951]. The aim is to minimise the cost function:

$$C_{SNE} = \sum_i KL(P_i||Q_i) = \sum_i \sum_j p_{ij} \log \frac{p_{ij}}{q_{ij}}$$

Hinton and Roweis [2003] assumed a Gaussian distribution in computing the similarity between two points in both high and low dimensional spaces. van der Maaten and Hinton [2008] proposed a variant of SNE, called t-SNE, which uses a symmetric version of SNE and a Student t-distribution to compute the similarity between two points in the low-dimensional space  $Q$ , given by

$$q_{ij} = \frac{(1 + \|\mathbf{y}_i - \mathbf{y}_j\|^2)^{-1}}{\sum_{k \neq l} (1 + \|\mathbf{y}_k - \mathbf{y}_l\|^2)^{-1}}$$

T-SNE is often preferred, because it reduces the effect of crowding problem (limited area to accommodate all data points and differentiate clusters) and it is easier to optimise, as it provides simpler gradients than SNE [van der Maaten and Hinton, 2008].

We propose *multi-SNE*, a multi-view manifold learning algorithm based on t-SNE. Our proposal computes the KL-divergence between the distribution of a single low-dimensional embedding and each data-view of the data separately, and minimises their weighted sum. An iterative algorithm is proposed, in which at each iteration the induced embedding is updated by minimising the cost function:

$$C_{\text{multi-SNE}} = \sum_m \sum_i \sum_j w^m p_{ij}^m \log \frac{p_{ij}^m}{q_{ij}}, \quad (1)$$

where  $w^m$  is the combination coefficient of the  $m^{\text{th}}$  data-view. The vector  $\mathbf{w} = (w^1, \dots, w^M)$  acts as a weight vector that satisfies  $\sum_m w^m = 1$ . In this study, equal weights on all data-views were considered, i.e.  $w^m = \frac{1}{M}$ ,  $\forall m = 1, \dots, M$ . The proposed multi-SNE approach is described in the Appendix.

An alternative multi-view extension of t-SNE, called *m-SNE* was proposed by Xie et al. [2011]. M-SNE applies t-SNE on a single distribution in the high-dimensional space, which is computed by combining the probability distributions of the data-views, given by  $p_{ij} = \sum_{m=1}^M \beta^m p_{ij}^m$ . The coefficients (or weights)  $\beta^m$  share the same role as  $w^m$  in multi-SNE and similarly  $\beta = (\beta^1, \dots, \beta^M)$  satisfies  $\sum_m \beta^m = 1$ . This leads to a different cost function than the one in equation (1).

In multi-SNE, we seek to avoid combining the probability distributions of all data-views together. Instead, it updates the induced embeddings by minimising the KL-divergence between every data-view's probability distribution and that of the low-dimensional representation we seek to obtain. In other words, this is achieved by computing and summing together the gradient descent for each data-view. The induced embedding is then updated by minimising the summed gradient descent.

### 2.3 Multi-LLE

LLE attempts to discover a non-linear structure of high-dimensional data,  $X$ , by computing low-dimensional and neighbourhood-preserving embeddings,  $Y$  [Saul and Roweis, 2001]. The main three steps of the algorithm are:

1. The set, denoted by  $\Gamma_i$ , contains the  $K$  nearest neighbours of each data point  $\mathbf{x}_i, i = 1, \dots, N$ . The most common distance measure between the data points is the Euclidean distance. Other local metrics can also be used in identifying the nearest neighbours [Roweis and Saul, 2000].
2. A weight matrix,  $W$ , is computed, which acts as a bridge between the high-dimensional space in  $X$  and the low-dimensional space in  $Y$ . Initially,  $W$  reconstructs  $X$ , by minimising the cost function:

$$\mathcal{E}_X = \sum_i |\mathbf{x}_i - \sum_j W_{ij} \mathbf{x}_j|^2 \quad (2)$$

where the weights  $W_{ij}$  describe the contribution of the  $j^{\text{th}}$  data point to the  $i^{\text{th}}$  reconstruction. The optimal weights  $W_{ij}$  are found by solving the least squares problem given in equation (2) subject to the constraints:

- (a)  $W_{ij} = 0$ , if  $j \notin \Gamma_i$ , and
  - (b)  $\sum_j W_{ij} = 1$
3. Once  $W$  is computed, the low-dimensional embedding  $\mathbf{y}_i$  of each data point  $i = 1, \dots, N$ , is obtained by minimising:

$$\mathcal{E}_Y = \sum_i |\mathbf{y}_i - \sum_j W_{ij} \mathbf{y}_j|^2 \quad (3)$$

The solution to equation (3), is obtained by taking the bottom  $d$  non-zero eigenvectors of the sparse  $N \times N$  matrix,  $M = (I - W)^T(I - W)$  [Roweis and Saul, 2000].

We propose *multi-LLE*, a multi-view extension of LLE, that computes the low-dimensional embeddings by using the consensus weight matrix:

$$\hat{W} = \sum_m \alpha^m W^m$$

where  $\sum_m \alpha^m = 1$ , and  $W^m$  is the weight matrix for each data-view  $m = 1, \dots, M$ . Thus,  $\hat{Y}$  is obtained by solving:

$$\mathcal{E}_{\hat{Y}} = \sum_i |\hat{\mathbf{y}}_i - \sum_j \hat{W}_{ij} \hat{\mathbf{y}}_j|^2$$

Shen et al. [2013] proposed *m-LLE*, an alternative multi-view extension of LLE. The LLE embeddings of each data-view are combined and LLE is applied on each data-view separately. The weighted average of those embeddings are taken as the unified low-dimensional embedding. In other words, computing the weight matrices  $W^m$  and solving  $\mathcal{E}_{Y^m} = \sum_i |\mathbf{y}_i^m - \sum_j W_{ij}^m \mathbf{y}_j^m|^2$ , for each  $m = 1, \dots, M$  separately. Thus, the low-dimensional embedding  $\hat{Y}$  is computed by  $\hat{Y} = \sum_m \beta^m Y^m$ , where  $\sum_m \beta^m = 1$ .

In contrast to m-LLE, multi-LLE combines the weight matrices obtained from each data-view, instead of the LLE embeddings. The multi-LLE algorithm is presented in the Appendix.

## 2.4 Multi-ISOMAP

ISOMAP aims to discover a low-dimensional embedding of high-dimensional data by maintaining the geodesic distances between all points [Tenenbaum et al., 2000]; it is often regarded as an extension of Multi-dimensional Scaling [Kruskal, 1964]. The ISOMAP algorithm comprises of the following three steps:

- Step 1. **A graph is defined.** Let  $G \sim (V, E)$  define a neighbourhood graph, with vertices  $V$  representing all data points. The edge length between any two vertices  $i, j \in V$  is defined by the distance metric  $d_X(i, j)$ , measured by the Euclidean distance. If a vertex  $j$  does not belong to the  $K$  nearest neighbours of  $i$ , then  $d_X(i, j) = 0$ . The parameter  $K$  is given as input, and it represents the connectedness of the graph  $G$ ; as  $K$  increases, more vertices are connected.
- Step 2. **The shortest paths between all pairs of points in  $G$  are computed.** The shortest path between vertices  $i, j \in V$  is defined by  $d_G(i, j)$ . Let  $D_G \in \mathbb{R}^{|V| \times |V|}$  be a matrix containing the shortest paths between any vertices  $i, j \in V$ , defined by  $(D_G)_{ij} = d_G(i, j)$ .  
The most efficient known algorithm to perform this task is Dijkstra’s Algorithm [Dijkstra, 1959]. In large graphs, an alternative approach to Dijkstra’s Algorithm would be to initialize  $d_G(i, j) = d_X(i, j)$  and replace all entries by  $d_G(i, j) = \min \{d_G(i, k), d_G(k, j)\}$ .
- Step 3. **The low-dimensional embeddings are constructed.** The  $i^{\text{th}}$  component of the low-dimensional embedding is given by  $y_i = \sqrt{\lambda_p} u_p^i$ , where  $\lambda_p$  is the  $p^{\text{th}}$  eigenvalue in decreasing order of the the matrix  $D_G$  and  $u_p^i$  the  $i^{\text{th}}$  component of  $p^{\text{th}}$  eigenvector [Tenenbaum et al., 2000].

Multi-ISOMAP is our proposal for adapting ISOMAP on multi-view data. Let  $G_m \sim (V, E_m)$  be a neighbourhood graph obtained from data-view  $X^{(m)}$  as defined in the first step of ISOMAP. All neighbourhood graphs are then combined into a single graph,  $\tilde{G}$ ; the combination is achieved by computing the edge length as the averaged distance of each data-view, *i.e.*  $d_{\tilde{G}}(i, j) = w_m \sum_m d_{G_m}(i, j)$ . Once a combined neighbourhood graph is computed, multi-ISOMAP follows steps 2 and 3 of ISOMAP described above. For simplicity, the weights throughout this paper were set as  $w_m = \frac{1}{M}, \forall m$ . The multi-ISOMAP algorithm is presented in the Appendix.

For completion, we have in addition adapted ISOMAP for multi-view visualisation following the framework of both m-SNE and m-LLE. Following the same logic, *m-ISOMAP* combines the ISOMAP embeddings of each data-view by taking the weighted average of those embeddings as the unified low-dimensional embedding. In other words, the low-dimensional embedding  $\hat{Y}$  is obtained by computing  $\hat{Y} = \sum_m \beta^m Y^m$ , where  $\sum_m \beta^m = 1$ .

## 2.5 Parameter Tuning

The multi-view manifold learning algorithms were tested on real and synthetic data sets for which the samples can be separated in several clusters. The true clusters are known and they were used to tune the parameters of the methods. To quantify the clustering performance, we used the following four extrinsic measures: (i) Accuracy (ACC), (ii) Normalised Mutual Information (NMI) [Vinh et al., 2010], (iii) Rand Index (RI) [Rand, 1971] and (iv) Adjusted Rand Index (ARI) [Hubert and Arabie, 1985]. All measures take values in the range  $[0, 1]$ , with 0 expressing complete randomness, and 1 perfect separation between clusters. The mathematical formulas of the four measures are presented in the Appendix.

SNE, LLE and ISOMAP depend on parameters that their proper tuning ensues to optimal results. LLE and ISOMAP depend on the number of nearest neighbours ( $NN$ ). SNE depends on the Perplexity ( $Perp$ ) parameter, which is directly

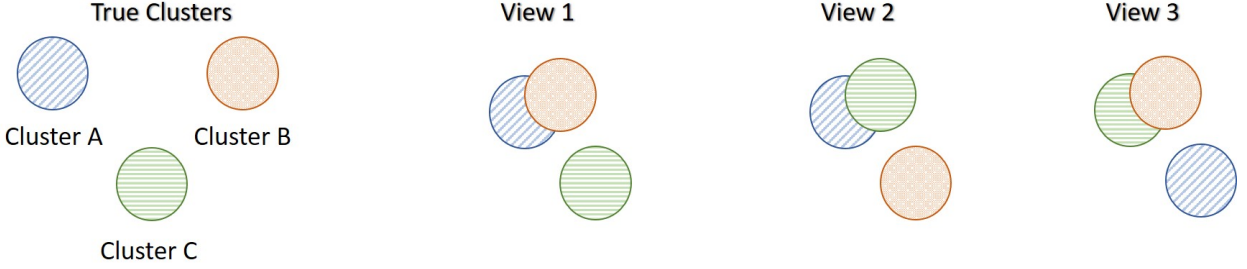


Figure 1: **Motivational Multi-view Data Scenario (MMDS)**. Each data-view captures different characteristics of the three clusters, and thus produces different clusterings.

related with the number of nearest neighbours. Similarly, the multi-view extensions of the three methods depend on the same parameters. The choice of the parameter can influence the visualisations and in some cases present the data into separate maps [van der Maaten and Hinton, 2012].

Assuming that the data samples belong to a number of clusters that we seek to identify, the performance of the algorithms was measured in a range of tuning parameter values,  $S = \{2, 10, 20, 50, 80, 100, 200\}$ . Note that for all algorithms, the parameter value cannot exceed the total number of samples in the data.

For all manifold learning approaches, the following procedure was implemented to tune the optimal parameters of each method per data set:

1. The method was applied with the different parameter values in  $S$ .
2. The  $K$ -means algorithm was applied on the low-dimensional embeddings produced by the chosen method.
3. The performance of the chosen method was evaluated quantitatively by computing ACC, NMI, RI and ARI for all tested parameter values.

The optimal parameter value is finally selected based on the evaluation measures. Section 4.3 explores how the different approaches are affected by the parameter values. In the remaining subsections of Section 4, the optimal parameter choice was used. If the truth is unknown, qualitative evaluation of the resulting visualisations can be performed instead.

### 3 Data

Data sets with different characteristics were analysed to explore and compare the proposed multi-view manifold learning algorithms under different scenarios (Table 1). The methods were evaluated on data sets that have different number of data-views, clusters and sample sizes. The real data sets analysed are classified as heterogeneous, due to the nature of their data, while the synthetic data sets are classified as non-heterogeneous, since they were generated under the same conditions and distributions. Both high-dimensional ( $p \gg N$ ) and low-dimensional data sets were analysed. Through these comparisons we wanted to investigate how the multi-view methods perform and how they compare with single-view methods.

In this section we describe the synthetic and real data sets analysed in the manuscript. Some of the real data sets analysed have previously been used in the literature for examining different multi-view algorithms, for example data integration [Wang et al., 2014] and clustering [Ou et al., 2018].

#### 3.1 Synthetic Data

A motivational multi-view example was constructed to qualitatively evaluate the performance of multi-view manifold learning algorithms against their corresponding single-view algorithms. Its framework was designed specifically to produce distinct projections of the samples from each data-view. Additional synthetic data sets were generated to explore how the algorithms behave when the separation between the clusters exists, but it is not as explicit as in the motivational example.

All synthetic data were generated using the following procedure. For the same set of samples, a specified number of data-views were generated, with each data-view capturing different information of the samples. Each sample follows a normal distribution with mean  $\mu$  and standard deviation  $\sigma = 1$ . For each data-view, different  $\mu$  values were chosen to

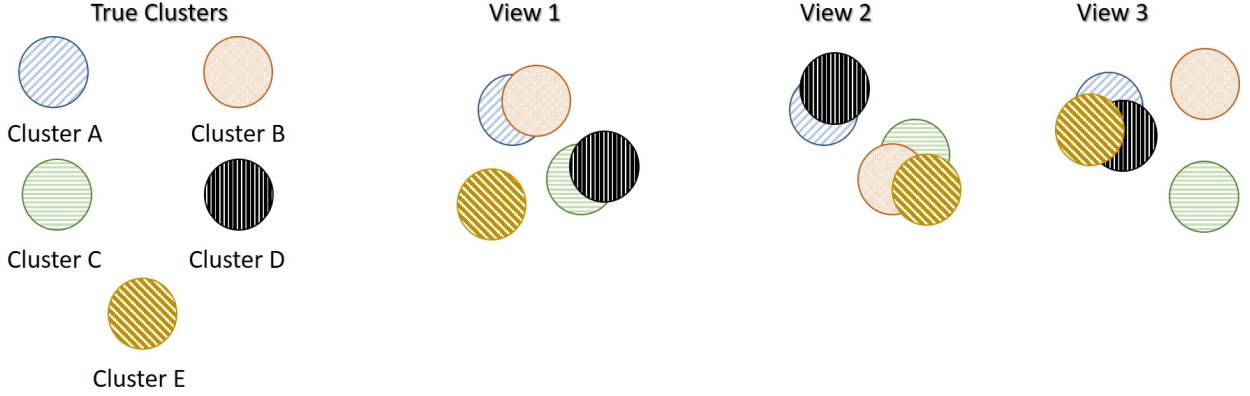


Figure 2: **More Clusters than data-views Scenario (MCS)**. In this example, there are 3 data views but 5 true underlying clusters. Each data-view captures different characteristics of the five clusters, and thus produces different clusterings.

distinguish the clusters. Noise, following a normal distribution with mean  $\mu_\epsilon = 0$  and standard deviation  $\sigma_\epsilon = 1$ , was added to increase randomness within each data-view. In other words,  $\mathbf{x}_i \sim MVN(\mu, 1) + \epsilon$ , where to each data-view and cluster, a different  $\mu$  was assigned, and  $\epsilon \sim N(0, 1)$ . Polynomial functions (e.g.  $h(x) = x^4 + 3x^2 + 5$ ) were applied on the samples to express non-linearity. The last step was performed to ensure that linear dimensionality reduction methods (e.g. PCA) would not successfully cluster the data.

### 3.1.1 Motivational Multi-view Data Scenario (MMDS)

Assume that the truth underlying structure of the data separates the samples into three true clusters as presented in Figure 1. Each synthetic data-view describes the samples differently, which results in three distinct clusterings, none of which reflects the global underlying truth. In particular, the first view separates only cluster C from the others (View 1 in Figure 1), the second view separates only cluster B (View 2) and the third view separates only cluster A (View 3).

### 3.1.2 Noisy data-view scenario (NDS)

A synthetic data set which consists of 4 data-views and 3 true underlying clusters was generated. The first three data-views follow the same structure as MMDS, while the 4<sup>th</sup> data-view represents a completely noisy data-view, *i.e.* with all data points lying in a single cluster. The rationale for creating such a data set is to examine the effect of the noisy data views in the multi-view visualisation and clustering. This data set was used to show that the multi-view approaches can identify not useful data-views and discard them. For  $n = 300$  equally balanced data samples, the data-views contain  $p_m = 100, \forall m = 1, 2, 3, 4$ , features. To summarise, NDS adds a noisy data-view to the MMDS data set.

### 3.1.3 More clusters than data-views scenario (MCS)

A synthetic data set that was generated similarly to MMDS but with 5 true underlying clusters instead of 3. The true underlying structure of the each data-view is shown in Figure 2. In this data set,  $p_v = 100, \forall v$  features were generated on  $n = 500$ , equally balanced data samples. In comparison with MMDS, MCS contains more clusters, but the same number of data-views.

## 3.2 Real Data

The real data sets analysed in the study are presented next.

### 3.2.1 Cancer Types<sup>2</sup>

This data set includes 65 patients with breast cancer, 82 with kidney cancer and 106 with lung cancer. For each patient the three data-views are available: (a) genomics ( $p_1 = 10299$  genes), (b) epigenomics ( $p_2 = 22503$  methylation sites)

<sup>2</sup><http://compbio.cs.toronto.edu/SNF/SNF/Software.html>

Data Description		Views	Clusters	Features	Samples	Hetero- geneous	High dimensional
	Data Set	( $M$ )	( $k$ )	( $p_{largest}$ )	( $N$ )		
Real	Cancer Types	3	3	22503	253	✓	✓
	Caltech7	6	7	1984	1474	✓	✓
	Handwritten Digits	6	10	240	2000	✓	✗
Synthetic	MMDS	3	3	300	300	✗	✗
	NDS	4	3	400	300	✗	✓
	MCS	3	5	300	500	✗	✗

Table 1: **The characteristics of the data sets analysed.** The number of views, number of clusters, the largest number of features amongst the data views, and the number of samples for both the real and synthetic data sets analysed are presented. Real data are taken as heterogeneous, whereas the synthetic data are regarded as homogeneous.

and (c) transcriptomics ( $p_3 = 302$  mi-RNA sequences). The aim is to cluster patients by their cancer type [Wang et al., 2014].

### 3.2.2 Caltech7<sup>3</sup>

Caltech-101 contains pictures of objects belonging to 101 categories. This publicly available subset of Caltech-101 contains 7 classes. It consists of 1474 objects on six data-views: (a) Gabor ( $p_1 = 48$ ), (b) wavelet moments ( $p_2 = 40$ ), (c) CENTRIST ( $p_3 = 254$ ), (d) histogram of oriented gradients ( $p_4 = 1984$ ), (e) GIST ( $p_5 = 512$ ), and (f) local binary patterns ( $p_6 = 928$ ) [Fei-Fei et al., 2006].

### 3.2.3 Handwritten Digits<sup>4</sup>

This data set consists of features on handwritten numerals (0 – 9) extracted from a collection of Dutch utility maps. Per class 200 patterns have been digitised in binary images (in total there are 2000 patterns). These digits are represented in terms of six data-views: (a) Fourier coefficients of the character shapes ( $p_1 = 76$ ), (b) profile correlations ( $p_2 = 216$ ), (c) Karhunen-Love coefficients ( $p_3 = 64$ ), (d) pixel averages in  $2 \times 3$  windows ( $p_4 = 240$ ), (e) Zernike moments ( $p_5 = 47$ ) and (f) morphological features ( $p_6 = 6$ ) [Dua and Graff, 2017].

The handwritten digits data set is characterised by having perfectly balanced data samples; each of the ten clusters contains exactly 200 numerals. On the other hand, caltech7 is an imbalanced data set with the first two clusters containing many more samples than the other clusters. The number of samples in each cluster is {A: 435, B: 798, C: 52, D: 34, E: 35, F: 64, G: 56}. The performance of the methods was explored on both the imbalanced caltech7 data set and a balanced version of the data, for which 50 samples from clusters *A* and *B* were randomly selected.

## 4 Results

In this section, we illustrate the application and evaluation of the proposed multi-view extensions of t-SNE, LLE and ISOMAP on real and synthetic data. In the following subsections we have addressed the following:

- 1. Can multi-view manifold learning approaches obtain better visualisations than single-view approaches?** The performance of the multi-view approaches in visualising the underlying structure of the data is illustrated. It is shown how the underlying structure is misrepresented when individual data sets or the concatenated data set are visualised.
- 2. The visualisations of multi-view approaches are quantitatively evaluated using  $K$ -means.** By extracting the low dimensional embeddings of the multi-view approaches and inputting them as features in the clustering algorithm  $K$ -means, we have quantitatively evaluated the performance of the approaches for identifying underlying clusters and patterns within the data.
- 3. The effect of the parameter values on the multi-view manifold learning approaches was explored.** As discussed the proposed multi-view manifold approaches depend on a parameter that requires tuning. In a series of experiments we investigated the effect that the parameter value has on each approach. This was done by

<sup>3</sup><https://github.com/yeqinglee/mvdata>

<sup>4</sup><https://archive.ics.uci.edu/ml/datasets/Multiple+Features>

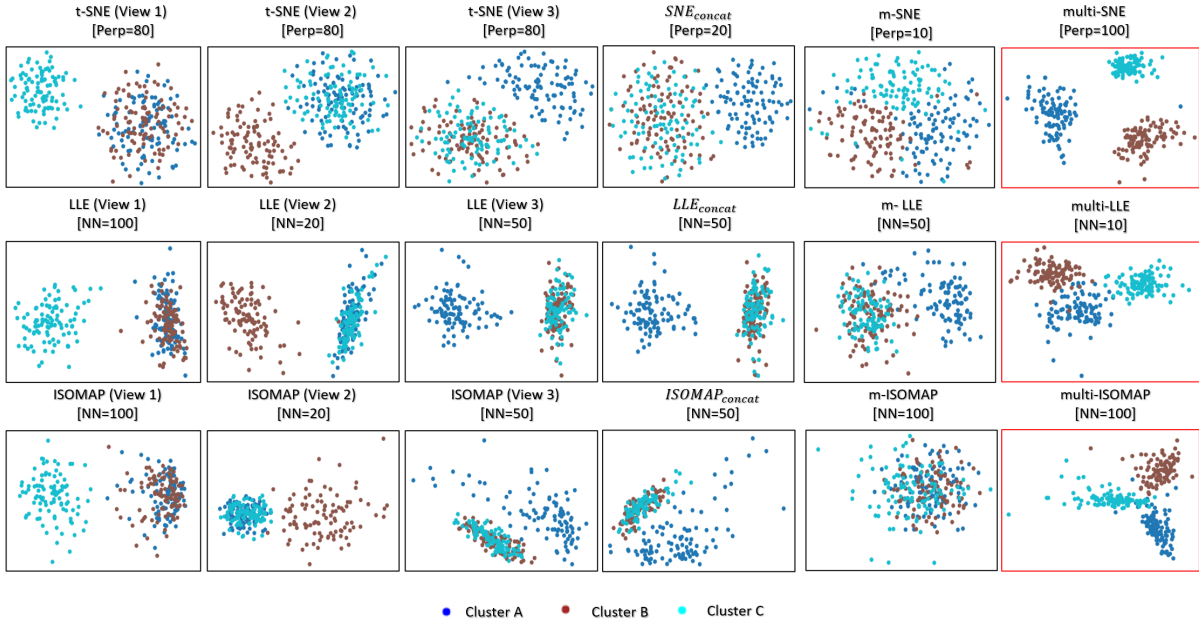


Figure 3: **Visualisations of MMDS.** Projections produced by the SNE, LLE, ISOMAP based algorithms. The projections within the red frames present our proposed methods: multi-SNE, multi-LLE and multi-ISOMAP. The parameters  $Perp$  and  $NN$  refer to the optimised perplexity and number of nearest neighbours, respectively.

exploring both the visualisations produced and by evaluating the clustering of the approaches for different parameter values.

4. **Should we use all available data-views? If some data-views contain more noise than signal, should we discard them?** These are two crucial questions that concern every researcher working with multi-view data; are all data-views necessary and beneficial to the final outcome? We have addressed these questions by analysing data sets that contain noisy data. By investigating both the produced visualisations and evaluating the clusterings obtained with and without the noisy data, we discuss why it is not always beneficial to include all available data views.

#### 4.1 Comparison Between Single-view and Multi-view Visualisations

Visualising multi-view data can be trivially achieved either by looking at the visualisations produced by each data-view, or by concatenating all features into a long vector. T-SNE, LLE and ISOMAP applied on each single data-view of the MMDS data set separately captures the correct local underlying structure of the respective data-view (Figure 3). However, by design they cannot capture the global structure of the data.  $SNE_{concat}$ ,  $LLE_{concat}$  and  $ISOMAP_{concat}$  represent the trivial solutions of concatenating the features of all data-views before applying t-SNE, LLE and ISOMAP, respectively. These trivial solutions capture mostly the structure of the third data-view, because that data-view has a higher variability between the clusters than the other two.

Multi-SNE, multi-LLE and multi-ISOMAP produced the best visualisations out of all SNE-based, LLE-based and ISOMAP-based approaches, respectively. These solutions were able to separate clearly the three true clusters, with multi-SNE showing the clearest separation between them. Even though m-SNE separates the samples according to their corresponding clusters, this separation would not be recognisable if the true labels were unknown, as the clusters are not sufficiently separated. The visualisation by m-LLE was similar to the ones produced by single-view solutions on concatenated features, while m-ISOMAP bundles all samples into a single cluster.

By visualising the MMDS data set via both single-view and multi-view clustering approaches, multi-SNE has shown the most promising results (Figure 3). We have shown that single-view analyses may lead to conflicting results, while multi-view approaches are able to capture the true underlying structure of the synthetic MMDS.

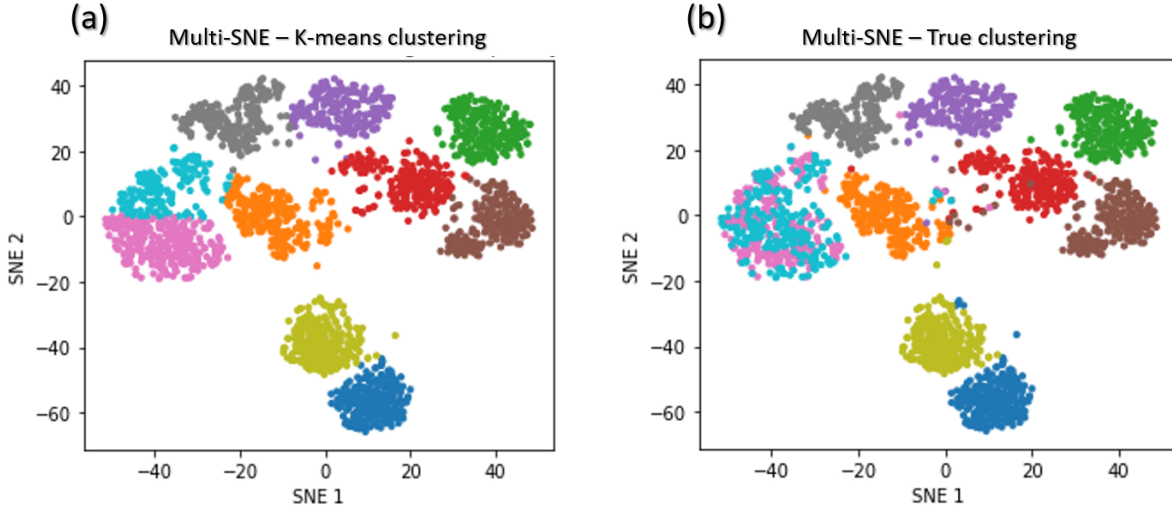


Figure 4: **Multi-SNE visualisations of handwritten digits.** Projections produced by multi-SNE with perplexity  $Perp = 10$ . Colours present the clustering on the data points by (a)  $K$ -means, and (b) Ground truth.

#### 4.2 Multi-view Manifold Learning for Clustering

It is very common in studies to utilise the visualisation of data to identify any underlying patterns or clusters within the data samples. Here, it is illustrated how the multi-view approaches can be used to identify such clusters. To quantify the visualisation of the data, we applied the  $K$ -means algorithm on the low-dimensional embeddings produced by multi-view manifold learning algorithms. If the two-dimensional embeddings can separate the data points to their respective clusters quantitatively with high accuracy via a clustering algorithm, then those clusters are expected to be qualitatively separated and visually shown in two dimensions.

For all examined data sets (synthetic and real), the number of clusters (ground truth) within the samples is known. The number of clusters was used as the input parameter,  $K$ , of the  $K$ -means algorithm and by computing the clustering measures we evaluated whether the correct sample allocations were made. The proposed multi-SNE, multi-LLE, and multi-ISOMAP approaches were found to outperform their competitive multi-view extensions (m-SNE, m-LLE, m-ISOMAP) as well as their concatenated versions ( $SNE_{concat}$ ,  $LLE_{concat}$ ,  $ISOMAP_{concat}$ ) (Table 2). For the majority of the data sets the multi-SNE approach was found to overall outperform all other approaches (Table 2).

Figure 4 shows a comparison between the true clusters of the handwritten digits data set and the clusters identified by  $K$ -means. The clusters reflecting the digits 6 and 9 are clustered together, but all remaining clusters are well separated and agree with the truth.

Multi-SNE applied on caltech7 produces a good visualisation, with clusters A and B being clearly separated from the rest (Figure 5b). Clusters C and G are also well-separated, but the remaining three clusters are bundled together. Applying  $K$ -means to that low-dimensional embedding does not capture the true structure of the data (Table 2). It provides a solution with all clusters being equally sized (Figure 5a) and thus its quantitative evaluation is misleading. Motivated by this result, we have further explored the performance of proposed approaches on a balanced version of the caltech7 data set (generated as described in Section 3.2).

Similarly to the visualisation of the original data set, the visualisation of the balanced caltech7 data set shows clusters A, B, C and G to be well-separated, while the remaining are still bundled together (Figures 5c and 5d).

Through the conducted work, it was shown that the multi-view approaches proposed in the manuscript generate low-dimensional embeddings that can be used as input features in a clustering algorithm (as for example the  $K$ -means algorithm) for identifying clusters that exist within the data set. We have illustrated that the proposed approaches outperform existing multi-view approaches and the visualisations produced by multi-SNE are very close to the ground truth of the data sets. Caution needs to be taken when data sets with imbalanced clusters are analysed as the quantitative performance of the approaches on such data sets is not very robust.

Data Set	Algorithm	Accuracy	NMI	RI	ARI
Handwritten Digits	SNE <sub>concat</sub> [Perp=10]	0.714	0.731	0.932	0.635
	m-SNE [Perp=10]	0.746	0.741	0.930	0.638
	<b>multi-SNE</b> [Perp=10]	<b>0.822</b>	<b>0.863</b>	<b>0.963</b>	<b>0.802</b>
	LLE <sub>concat</sub> [NN=10]	0.562	0.560	0.871	0.441
	m-LLE [NN=10]	<b>0.632</b>	0.612	0.896	0.503
	multi-LLE [NN=5]	0.614	<b>0.645</b>	<b>0.897</b>	<b>0.524</b>
	ISOMAP <sub>concat</sub> [NN=20]	0.634	0.619	0.905	0.502
	m-ISOMAP [NN=20]	0.636	0.628	0.898	0.477
multi-ISOMAP [NN=5]	<b>0.658</b>	<b>0.631</b>	<b>0.909</b>	<b>0.518</b>	
Caltech7	SNE <sub>concat</sub> [Perp=50]	0.398	0.311	0.676	0.226
	<b>m-SNE</b> [Perp=10]	<b>0.559</b>	<b>0.534</b>	<b>0.766</b>	<b>0.457</b>
	multi-SNE [Perp=80]	0.541	0.472	0.726	0.350
	LLE <sub>concat</sub> [NN=100]	0.434	0.283	0.792	0.188
	m-LLE [NN=5]	0.431	0.313	0.767	0.221
	multi-LLE [NN=80]	<b>0.513</b>	<b>0.380</b>	<b>0.788</b>	<b>0.264</b>
	ISOMAP <sub>concat</sub> [NN=20]	0.388	0.295	0.678	0.247
	m-ISOMAP [NN=5]	0.416	0.306	0.686	0.261
multi-ISOMAP [NN=10]	<b>0.521</b>	<b>0.354</b>	<b>0.727</b>	<b>0.367</b>	
Caltech7 (balanced)	SNE <sub>concat</sub> [Perp=80]	0.474	0.318	0.700	0.293
	m-SNE [Perp=10]	0.563	0.406	0.829	0.337
	<b>multi-SNE</b> [Perp=20]	<b>0.762</b>	<b>0.688</b>	<b>0.908</b>	<b>0.631</b>
	LLE <sub>concat</sub> [NN=20]	0.567	0.348	<b>0.725</b>	0.380
	m-LLE [NN=10]	0.403	0.169	0.617	0.139
	multi-LLE [NN=5]	<b>0.622</b>	<b>0.454</b>	0.71	<b>0.391</b>
	ISOMAP <sub>concat</sub> [NN=5]	0.434	0.320	0.791	0.208
	m-ISOMAP [NN=5]	0.455	0.299	0.797	0.224
multi-ISOMAP [NN=5]	<b>0.548</b>	<b>0.368</b>	<b>0.81</b>	<b>0.267</b>	
NDS	SNE <sub>concat</sub> [Perp=80]	0.747	0.628	0.817	0.598
	m-SNE [Perp=50]	0.650	0.748	0.766	0.629
	<b>multi-SNE</b> [Perp=80]	<b>0.989</b>	<b>0.951</b>	<b>0.969</b>	<b>0.987</b>
	LLE <sub>concat</sub> [NN=5]	0.606	0.477	0.684	0.446
	m-LLE [NN=20]	0.685	0.555	0.768	0.528
	multi-LLE [NN=20]	<b>0.937</b>	<b>0.768</b>	<b>0.922</b>	<b>0.823</b>
	ISOMAP <sub>concat</sub> [NN=100]	0.649	0.528	0.750	0.475
	m-ISOMAP [NN=5]	0.610	0.453	0.760	0.386
multi-ISOMAP [NN=300]	<b>0.778</b>	<b>0.788</b>	<b>0.867</b>	<b>0.730</b>	
MCS	SNE <sub>concat</sub> [Perp=200]	0.421	0.215	0.711	0.173
	m-SNE [Perp=2]	0.641	0.670	0.854	0.575
	<b>multi-SNE</b> [Perp=50]	<b>0.919</b>	<b>0.862</b>	<b>0.942</b>	<b>0.819</b>
	LLE <sub>concat</sub> [NN=50]	0.569	0.533	0.796	0.432
	m-LLE [NN=20]	0.540	0.627	0.819	0.487
	multi-LLE [NN=20]	<b>0.798</b>	<b>0.647</b>	<b>0.872</b>	<b>0.607</b>
	ISOMAP <sub>concat</sub> [NN=150]	0.628	0.636	0.834	0.526
	m-ISOMAP [NN=5]	0.686	<b>0.660</b>	0.841	0.565
multi-ISOMAP [NN=300]	<b>0.717</b>	0.630	<b>0.852</b>	<b>0.570</b>	

Table 2: **Clustering performance.** For each data set, **red** highlights the method with the best performance on each measure between each group of algorithms (SNE, LLE or ISOMAP based). The overall superior method for each data set is depicted with **bold**. The parameters *Perp* and *NN* refer to the selected perplexity and number of nearest neighbours, respectively. They were optimised for the corresponding methods.

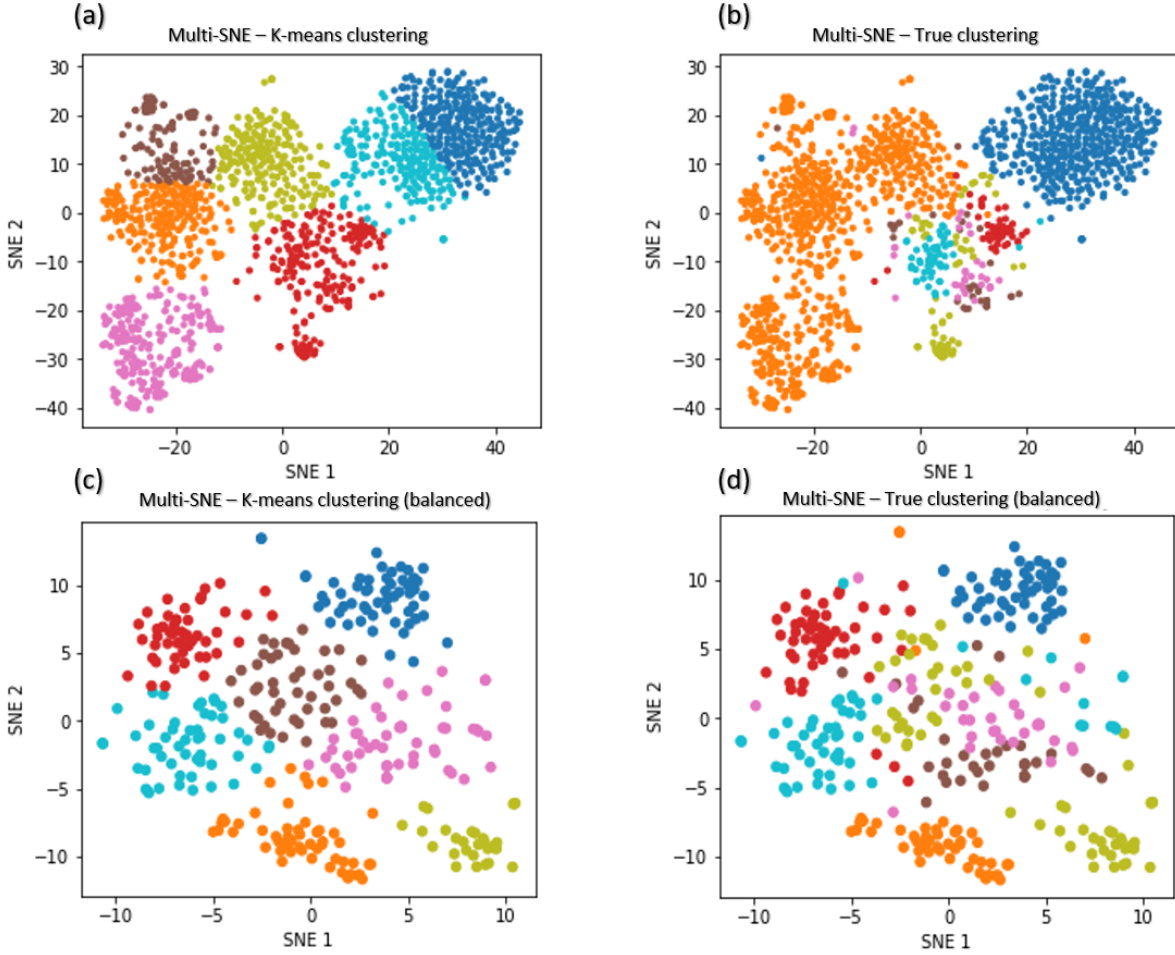


Figure 5: **Multi-SNE visualisations of caltech7 and its balanced subset.** Projections produced by multi-SNE with perplexity  $Perp = 80$  and  $Perp = 10$  for the original and balanced caltech7 data set, respectively. Colours present the clustering on the data points by (a), (c)  $K$ -means, and (b), (d) Ground truth. (a) (b) present the data points on the original caltech7 data set, while (c), (d) are on its balanced subset.

### 4.3 Optimal Parameter Selection

SNE, LLE and ISOMAP depend on a parameter that requires tuning. Even though the parameter is defined differently in each algorithm, it is always related to the nearest number of global neighbours. As described earlier, the optimal parameter was found by comparing the performance of the methods on a range of parameter values,  $S = \{2, 10, 20, 50, 80, 100, 200\}$ . In this section the synthetic data sets, NDS and MCS, were analysed, because both data sets separate the samples into known clusters by design and evaluation via clustering measures would be appropriate.

To find the optimal parameter value, the performance of the algorithms was evaluated by applying  $K$ -means on the low-dimensional embeddings and comparing the resulting clusterings against the truth. Once the optimal parameter was found, we confirmed that the clusters were visually separated by manually looking at the two-dimensional embeddings. Since the data in NDS and MCS are perfectly balanced and were generated for clustering, this approach can effectively evaluate the data visualisations.

On NDS, single-view SNE, LLE and ISOMAP algorithms produced a misclustering error of 0.3, meaning that a third of the samples was incorrectly clustered (Figure 6b). This observation shows that single-view methods capture the true local underlying structure of each synthetic data-view. The only exception for NDS is the fourth data-view, for which the error is closer to 0.6, *i.e.* randomly assigns the clusters (which follows the simulation design, as it was designed to

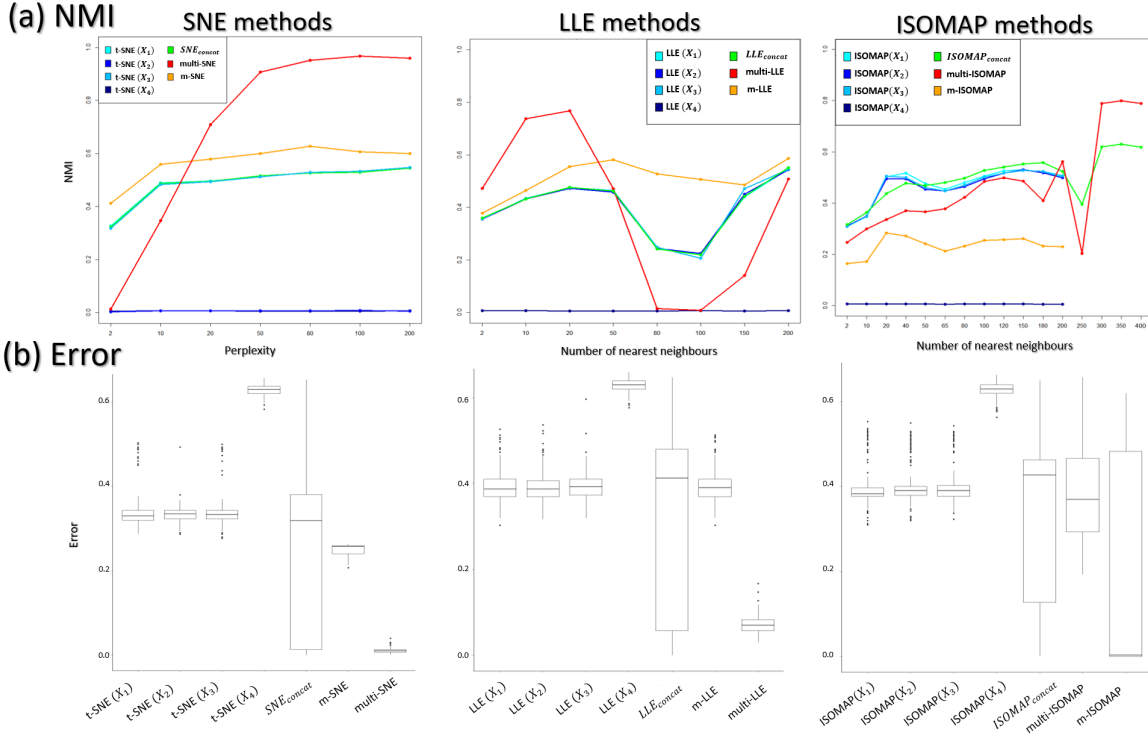


Figure 6: **NDS evaluation measures.** (a) NMI values along different parameter values on all manifold learning algorithms and (b) Misclustering error on the optimal parameter values.

be a random data-view). After concatenating the features of all data-views, the performance of single-view approaches remains poor (Figure 6a). The variance of the misclustering error on this solution is much greater, suggesting that single-view manifold learning algorithms on concatenated data are not robust and thus not reliable.

On both NDS and MCS, multi-LLE and multi-SNE were found to be sensitive to choice of their corresponding parameter value (Figures 6a and 7). While multi-LLE performed the best when the number of nearest neighbours was low, multi-SNE provided better results as perplexity was increasing. On the other hand, multi-ISOMAP had the highest NMI value when the parameter was high.

Overall, ISOMAP-based multi-view algorithms showed a higher variability than the other multi-view methods, which makes them less favourable solutions. The performance of ISOMAP-based methods improved as the parameter value increased (Figure 7). However, they were outperformed by multi-LLE and multi-SNE for both synthetic data sets.

Out of the three manifold learning foundations, LLE-based approaches depend the most on their parameter value to produce the optimal outcome. Specifically, their performance dropped when the parameter value lay between 20 and 100 (Figure 6a). When the number of nearest neighbours was set to be greater than 100 their performance started to improve. Out of all LLE-based algorithms, the highest NMI and lowest misclustering error was obtained by multi-LLE (Figures 6 and 7).

Even though, m-SNE performed better than single-view methods in terms of both clustering and error variability, multi-SNE produced the best results (Figures 6 and 7). In particular, multi-SNE outperformed all algorithms presented in this paper on both NDS and MCS. Even though it performed poorly for low perplexity values, its performance improved for  $Perp \geq 20$ . Multi-SNE was the algorithm with the lowest error variance, making it a robust and preferable solution.

#### 4.4 Optimal Number of Data-views

It is common to think that more information would lead to better results, and in theory that should be the case. However, in practice that is not always true [Kumar et al., 2011]. Using the cancer types data set, we explored whether the visualisations and clusterings are improved if all or a subset of the data-views are used. With three available data-views,

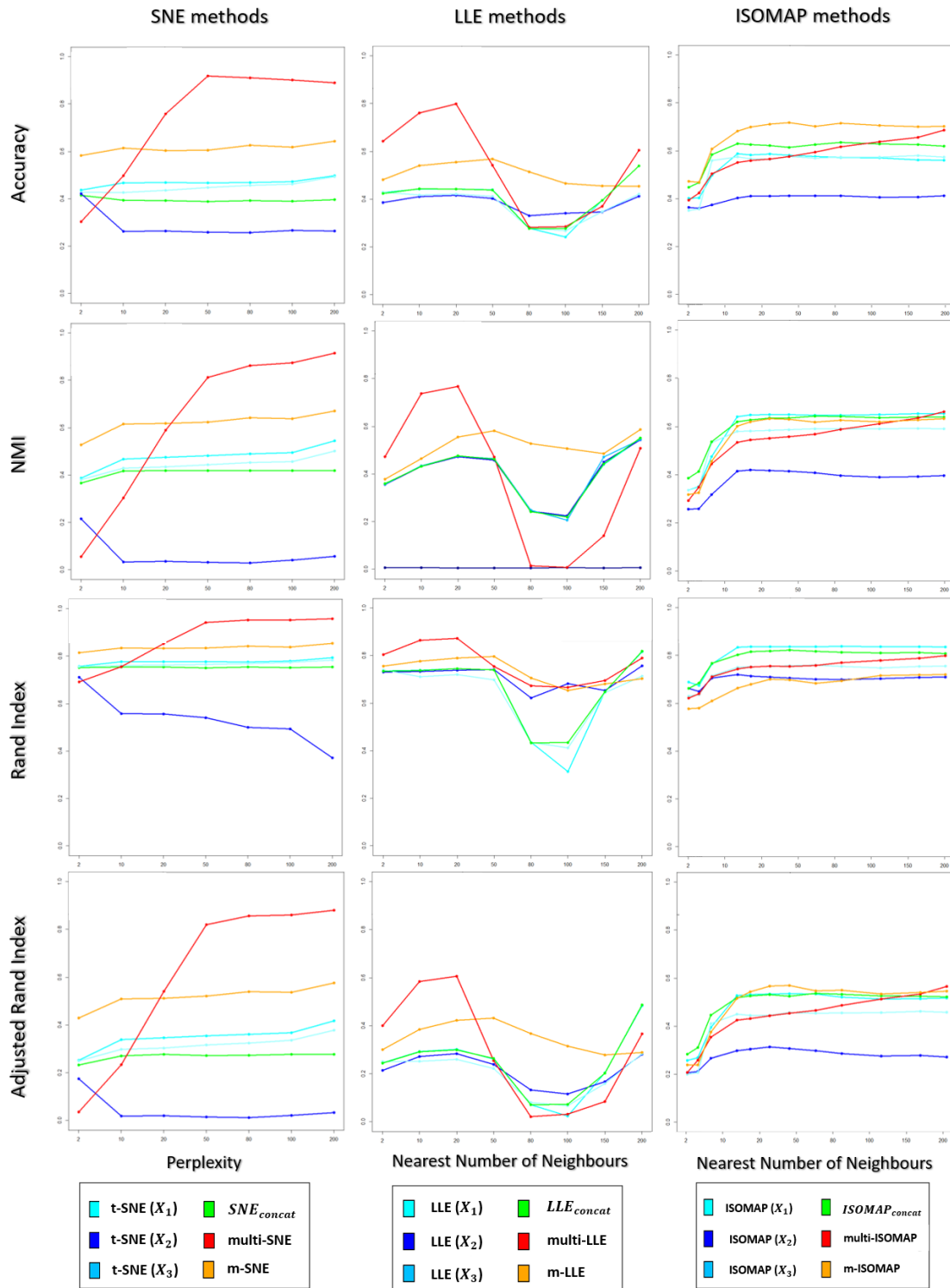


Figure 7: **MCS evaluation measures.** The clustering evaluation measures are plotted against different parameter values on the all SNE, LLE and ISOMAP based algorithms.

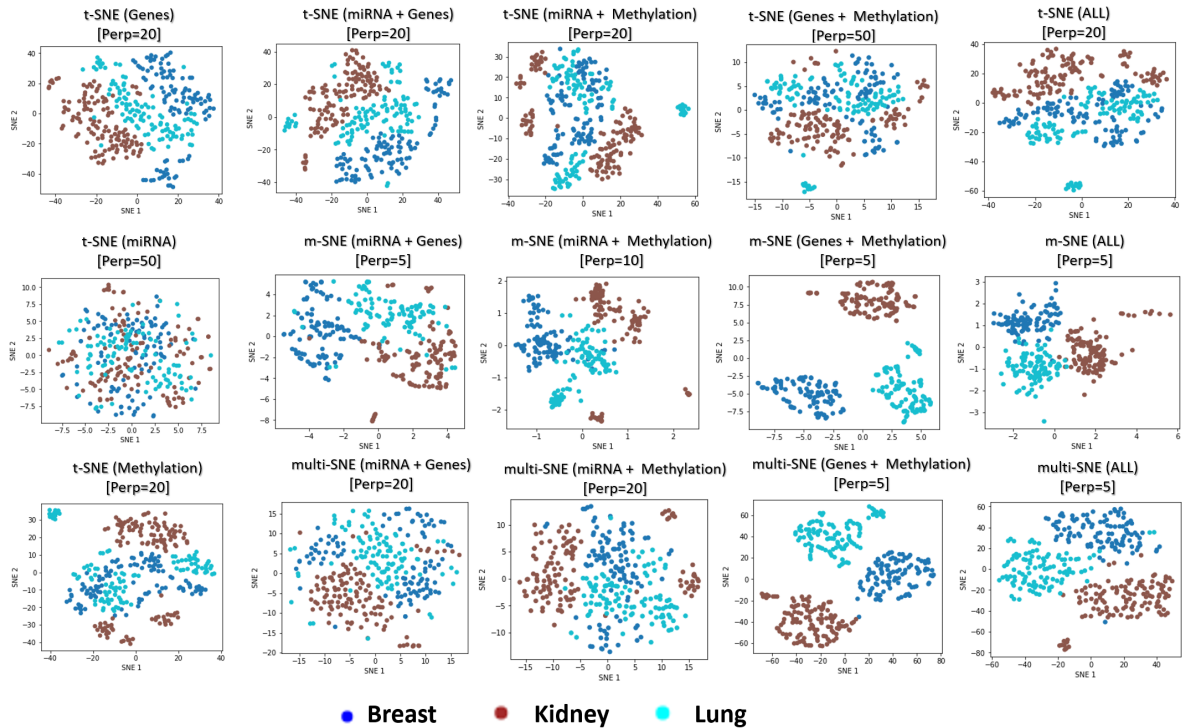


Figure 8: **Visualisations of cancer types.** Projections produced by all SNE-based manifold learning algorithms on all possible combinations between the three data-views in the cancer types data set. The parameter  $Perp$  refers to the selected perplexity, which was optimised for the corresponding methods.

we implemented a multi-view visualisation on three combinations of two data-views and a single combination of three data-views.

The genomics data-view provides a reasonably good separation of the three cancer types, whereas miRNA data-view fails in this task, as it provides a visualisation that reflects random noise (first column of plots in Figure 8). Concatenating features from the different data-views before implementing t-SNE does not improve the final outcome of the algorithm, regardless of the data-view combination.

Overall, multi-view manifold learning algorithms have improved the data visualisation to a great extent. When all three data-views are considered, both multi-SNE and m-SNE provide a good separation of the clusters (Figure 8). However, the true cancer types can be identified perfectly when the miRNA data-view is discarded. In other words, the optimal solution in this data set is obtained when only genomics and epigenomics data-views are used. That is because miRNA data-view contains little information about the cancer types and adds random noise, which makes the task of separating the data points more difficult.

This observation was also noted between the visualisations of MMDs and NDS (Figure 9). The only difference between the two synthetic data sets, is the additional noisy data-view in NDS. Even though NDS separates the samples to their corresponding clusters, the separation is not as clear as it is in the projection of MMDs via multi-SNE. In agreement with the exploration of the cancer types data set, it is favourable to discard any noisy data-views in the implementation of multi-view manifold learning approaches.

It is not always a good idea to include all available data-views in multi-view manifold learning algorithms; some data-views may provide noise which would result in a worse visualisation than discarding those data-views entirely. The noise of a data-view with unknown labels may be viewed in a single-view t-SNE plot (all data-points in a single cluster), or identified, if possible, via quantification measures such as signal-to-noise ratio.

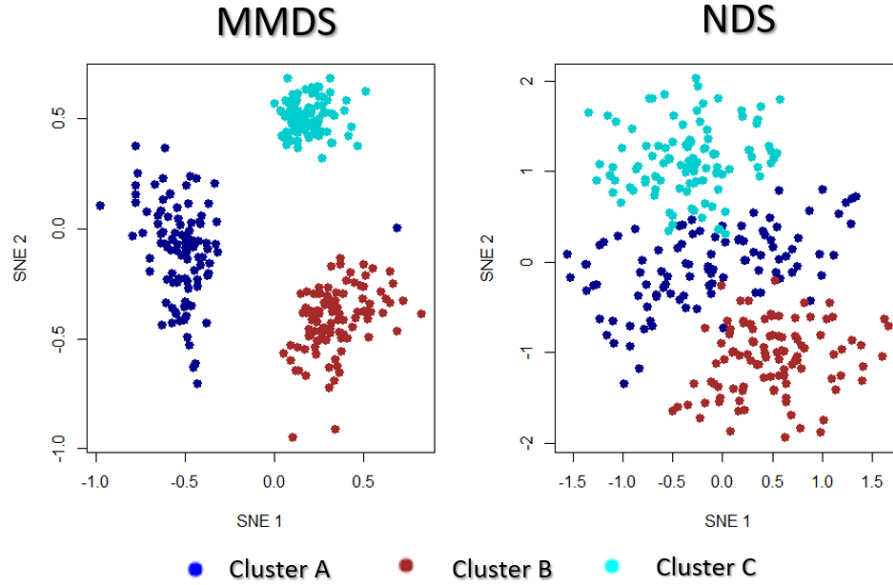


Figure 9: **Multi-SNE visualisations of MMDS and NDS.** Projections produced by multi-SNE with perplexity  $Perp = 100$  for both MMDS and NDS.

## 5 Discussion

In this manuscript we propose extensions of the well-known manifold learning approaches t-SNE, LLE, and ISOMAP for the visualisation of multi-view data sets. These three approaches are widely used for the visualisation of high-dimensional and complex data sets on performing non-linear dimensionality reduction. The increasing number of multiple data sets produced for the same samples in different fields, emphasises the need for approaches that produce expressive presentations of the data. We have illustrated that visualising each data set separately from the rest is not ideal as it does not reveal the underlying patterns within the samples. In contrast, the proposed multi-view approaches can produce a single visualisation of the samples by integrating all available information from the multiple data-views.

Multi-view visualisation has been explored in the literature with the m-SNE and m-LLE approaches recently proposed. In this work, we have explored alternative solutions to both m-SNE and m-LLE and extended these solutions for the ISOMAP approach. Through a comparative study of real and synthetic data we have illustrated that the proposed approach, multi-SNE, provides a better and more robust solution compared to m-SNE; similar results were obtained for multi-LLE and m-LLE.

We have utilised the low-dimensional embeddings of the proposed algorithms as features in the  $K$ -means clustering algorithm, which we have used (1) to quantify the visualisations produced, and (2) to select the optimal tuning parameters for the manifold learning approaches. By investigating synthetic and real multi-view data sets, each with different data characteristics, we concluded that multi-SNE provides a more accurate and robust solution than any other single-view and multi-view manifold learning algorithms we have considered. Specifically, multi-SNE was able to produce the best data visualisations of all data sets analysed in this paper. Multi-LLE provides the second best solution, while multi-view ISOMAP algorithms have not produced competitive visualisations. By exploring several data sets, we concluded that multi-view manifold learning approaches can be effectively applied on heterogeneous and high-dimensional data (*i.e.*  $p \gg n$ ).

Through the conducted experiments, we have illustrated the effect of the parameters on the performance of the methods. We have shown that SNE-based methods perform the best when perplexity is in the range  $[20, 100]$ , LLE-based algorithms should take a small number of nearest neighbours, in the range  $[10, 50]$ , while the parameter of ISOMAP-based should be in the range  $[100, N]$ , where  $N$  is the number of samples.

We demonstrated that in a multi-view setting taking all available data-views does not necessarily produce the best results. By investigating the cancer types data set, we recognised that if a data-view is more noisy, it is likely that the visualisation will worsen. It is preferable in such situations to discard the noisy data-view(s). An alternative approach is

Multi-view Clustering on handwritten digits data set									
	Kumar et al. (2011)	Liu et al. (2013)	Sun et al. (2015)	Ou et al. (2016)	Ou et al. (2018)	2D	multi-SNE		
							3D	5D	10D
NMI	0.768	0.804	0.876	0.785	0.804	0.863	<b>0.894</b>	<b>0.897</b>	<b>0.899</b>
ACC	–	<b>0.881</b>	–	0.876	<b>0.880</b>	0.822	0.848	0.854	0.849

Table 3: **Multi-view clustering performance on handwritten digits.** The NMI and accuracy (ACC) values of multi-view clustering approaches, as they were presented by the authors in their corresponding papers, are depicted along the clustering performance of multi-SNE on a range of dimensions for the embeddings ( $d = 2, 3, 5, 10$ ).

to adjust accordingly the weight vector of each data-view, changing the contribution of the data-view to the overall visualisation.

Multi-view clustering is a topic that has gathered a lot of interest in the recent years with a number of approaches published in the literature. Such approaches include the ones proposed by Kumar et al. [2011], Liu et al. [2013], Sun et al. [2015], Ou et al. [2016] and Ou et al. [2018]. The handwritten data set presented in the manuscript, has been analysed by the aforementioned studies for multi-view clustering. Table 3 shows the NMI and accuracy values of the clusterings performed by the multi-view clustering algorithms (these values are as given in the corresponding articles). In addition, the NMI and accuracy values of the  $K$ -means clustering applied on the multi-SNE low-dimensional embeddings (from 2 to 10 dimensions) are presented in the table. The performance of multi-SNE with  $K$ -means is found to be comparable with the multi-view clustering algorithms (Table 3). By applying  $K$ -means to the low-dimensional embeddings of multi-SNE can successfully cluster the observations of the data (see Appendix for a 3-dimensional visualisation via multi-SNE).

An important area of active current research, where manifold learning approaches, such as t-SNE, as visualisation tools are commonly used is single-cell sequencing (scRNA-seq) and genomics. Last few years, have seen fast developments of multi-omics single-cell methods, where for example for the same cells multiple omics measurements are being obtained such as transcripts by scRNA-seq and chromatin accessibility by a method known as scATAC-seq [Stuart et al., 2019]. As recently discussed the integration of this kind of multi-view single-cell data poses unique and novel statistical challenges [Argelaguet, 2021]. We therefore believe our proposed multi-view methods will be very useful in producing an integrated visualisation of cellular heterogeneity and cell types studied by multi-omics single-cell methods in different tissues, in health and disease.

To illustrate the capability of multi-SNE for multi-omics single-cell data, we applied multi-SNE on a representative data set of scRNA-seq and ATAC-seq for human peripheral blood mononuclear cells (PBMC) <sup>5</sup> [Stuart and Srivastava, 2021(@)] (Figure 7). To test the quality of the obtained multi-view visualisation, we compared its performance against the multi-view clustering approach proposed by Liu et al. [2013] on this single-cell data. A balanced subset of this data set was used, which consists of two data-views on 9105 cells (*scRNA-seq* and *ATAC-seq* with 36000 and 108000 features, respectively). A detailed description of this data set, the pre-processing steps performed, and the projections of t-SNE and multi-SNE on the original data are provided in the Appendix (Figure 11). We find Multi-SNE had the highest accuracy (and a close NMI to the approach by Liu et al. [2013]) as seen in Figure 7. Qualitatively, the projections by t-SNE on scRNA-seq and multi-SNE are similar, but multi-SNE separates the clusters better (especially between *CD4* and *CD8* cell types (Figure 7 and Figure 11 in Appendix). While it is known that ATAC-seq data is more noisy and has less information by itself, we see that integration of the data-views results in better overall separation of the different cell types in this data set. These results indicate the promise of multi-SNE as a unified multi-view and clustering approach for multi-omics single-cell data.

The increasing number of multi-view, high-dimensional and heterogeneous data requires novel visualisation techniques that integrate this data into expressive and revealing representations. In this manuscript, new multi-view manifold learning approaches are presented and their performance across real and synthetic data sets with different characteristics was explored. The multi-SNE approach is proposed to provide a unified solution for robust visualisation and subsequent clustering of multi-view data.

<sup>5</sup> [https://support.10xgenomics.com/single-cell-multiome-atac-gex/datasets/1.0.0/pbmc\\_granulocyte\\_sorted\\_10k](https://support.10xgenomics.com/single-cell-multiome-atac-gex/datasets/1.0.0/pbmc_granulocyte_sorted_10k)

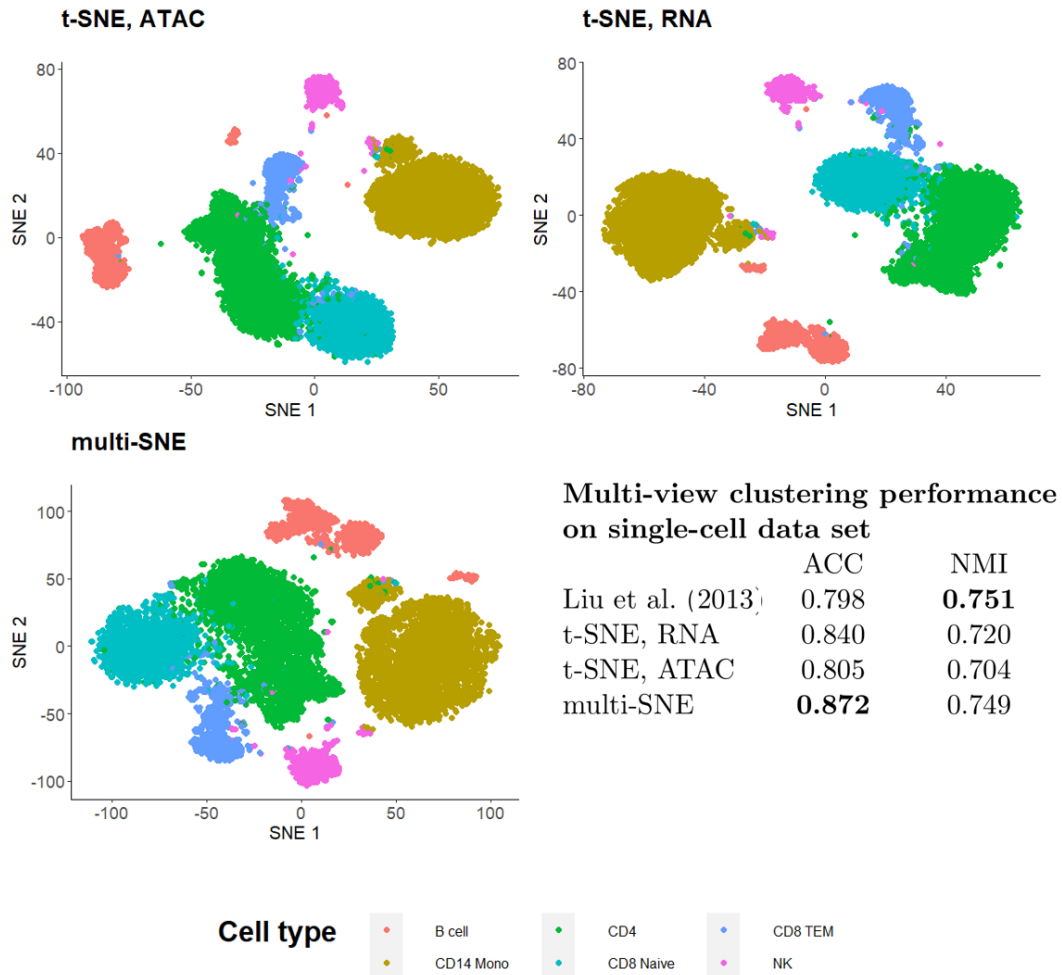


Figure 10: **Visualisations and clustering performance on single-cell multi-omics data.** Projections produced by t-SNE on RNA, ATAC and multi-SNE on both data-views with perplexity  $Perp = 80$  for the two t-SNE projections and  $Perp = 20$  for multi-SNE. The clustering performance of the data by Liu et al. [2013], t-SNE and multi-SNE are presented.

## References

- Ricard Argelaguet, Anna S. E. Cuomo, Oliver Stegle, John C. Marioni. Computational principles and challenges in single-cell data integration. *Nature Biotechnology*, 1546-1696, 2021.
- Stephen M. Casner. Task-analytic approach to the automated design of graphic presentations. *ACM Transactions on Graphics*, 10(2):111–151, 1991.
- Tat-Seng Chua, Jinhui Tang, Richang Hong, Haojie Li, Zhiping Luo, and Yan-Tao Zheng. Nus-wide: A real-world web image database from national university of singapore. In *Proceedings of the 2009 ACM International Conference on Image and Video Retrieval*, 2009.
- Dick de Ridder, Olga Kouropteva, Oleg Okun, Matti Pietikäinen, and Robert P. W. Duin. Supervised locally linear embedding. In *Artificial Neural Networks and Neural Information Processing 2003*, pages 333–341, 2003.
- Edsger W. Dijkstra. A note on two problems in connexion with graphs. *Numerische mathematik*, 1(1):269–271, 1959.
- Dheeru Dua and Casey Graff. UCI machine learning repository, 2017.
- Li Fei-Fei, Rob Fergus, and Perona Pietro. One-shot learning of object categories. *IEEE Transactions on Pattern Analysis and Machine Intelligence*, 28(4):594–611, 2006.
- Yun Fu, Liangliang Cao, Guodong Guo, and Thomas S. Huang. Multiple feature fusion by subspace learning. In *Proceedings of the 2008 International Conference on Content-Based Image and Video Retrieval*, page 127–134, 2008.
- Diego García, Ignacio Díaz, Daniel Pérez, Abel A. Cuadrado, Manuel Domínguez and Antonio Morá. Interactive visualization for NILM in large buildings using non-negative matrix factorization. *Energy and Buildings*, 17695–108, 2018.
- Patrick J.F Groenen and Ingwer Borg. The past, present, and future of multidimensional scaling. Econometric institute research papers, 2013.
- Yehudit Hasin, Marcus Seldin, and Aldons Lusic. Multi-omics approaches to disease. *Genome Biology*, 18, 2017.
- Geoffrey E. Hinton and Sam T. Roweis. Stochastic neighbor embedding. *Advances in Neural Information Processing Systems*, pages 857–864, 2003.
- Paul Hoffman, Satija Lab and Collaborators. Integrating scRNA-seq and scATAC-seq data. [https://satijalab.org/seurat/articles/atacseq\\_integration\\_vignette.html](https://satijalab.org/seurat/articles/atacseq_integration_vignette.html), 2021, Accessed: 2021-03-18.
- Lawrence Hubert and Phipps Arabie. Comparing partitions. *Journal of Classification*, 2:193–218, 1985.
- Kanghua Hui and Chunheng Wang. Clustering-based locally linear embedding. In *2008 19th International Conference on Pattern Recognition*, pages 1–4, 2008.
- Ian T. Jolliffe and Jorge Cadima. Principal component analysis: A review and recent developments. In *Philosophical Transactions the Royal Society A* 374, 2016.
- Joseph B. Kruskal. Multidimensional scaling by optimizing goodness of fit to a nonmetric hypothesis. In *Psychometrika* 29:1–27, 1964.
- Solomon Kullback and Richard A. Leibler. On information and sufficiency. 22:79–86, 1951.
- Abhishek Kumar, Piyush Rai, and Daume Hal. Co-regularized multi-view spectral clustering. In *Advances in Neural Information Processing Systems 24*, pages 1413–1421, 2011.
- Gen Li, Xiaokang Liu, and Kun Chen. Integrative multi-view regression: Bridging group-sparse and low-rank models. *Biometrics*, 75:593 – 602, 2019.
- Mingai Li, Xinyong Luo, Jinfu Yang, and Yanjun Sun. Applying a locally linear embedding algorithm for feature extraction and visualization of mi-eeg. *Journal of Sensors*, 2016, 2016.
- Xiangyuan Li, Cheng Cai, and Jinrong He. Density-based multi-manifold isomap for data classification. In *2017 Asia-Pacific Signal and Information Processing Association Annual Summit and Conference (APSIPA ASC)*, pages 897–903, 2017.
- George C. Linderman and Stefan Steinerberger. Clustering with t-sne, provably. *SIAM Journal on Mathematics of Data Science*, 1(2):313–332, 2019.
- Jialu Liu, Chi Wang, Jing Gao, and Jiawei Han. Multi-view clustering via joint nonnegative matrix factorization. *Proceedings of the 2013 SIAM International Conference on Data Mining*, pages 252–260, 2013.
- James MacQueen. Some methods for classification and analysis of multivariate observations. *Proceedings of the fifth Berkeley symposium on mathematical statistics and probability*, 1(14):281–297, 1967.

- Leland McInnes, John Healy, Nathaniel Saul, and Lukas Großberger. Umap: Uniform manifold approximation and projection. *Journal of Open Source Software*, 3(29):861, 2018.
- Andrew Y. Ng, Michael I. Jordan, and Yair Weiss. On spectral clustering: analysis and an algorithm. In *Proceedings of the Fourteenth International Conference on Neural Information Processing Systems: Natural and Synthetic*, pages 849–856, 2001.
- Weihua Ou, Shujian Yu, Gai Li, Jian Lu, Kesheng Zhang, and Gang Xie. Multi-view non-negative matrix factorization by patch alignment framework with view consistency. *Neurocomputing*, 204:116 – 124, 2016.
- Weihua Ou, Fei Long, Yi Tan, Shujian Yu, and Wang Pengpeng. Co-regularized multiview nonnegative matrix factorization with correlation constraint for representation learning. *Multimedia Tools and Applications*, 77:12955–12978, 2018.
- William M. Rand. Objective criteria for the evaluation of clustering methods. *Journal of the American Statistical Association*, 66(336):846–850, 1971.
- Theodoulos Rodosthenous, Vahid Shahrezaei and Marina Evangelou Integrating multi-OMICS data through sparse canonical correlation analysis for the prediction of complex traits: a comparison study *Bioinformatics*, 36(17): 4616-4625, 2020.
- Sam T. Roweis and Lawrence K. Saul. Nonlinear dimensionality reduction by locally linear embedding. *Science*, 290: 2323–2326, 2000.
- Lawrence Saul and Sam Roweis. An introduction to locally linear embedding. *Journal of Machine Learning Research*, 7, 01 2001.
- Erich Schubert and Michael Gertz. Intrinsic t-stochastic neighbor embedding for visualization and outlier detection. In *Similarity Search and Applications*, pages 188–203, 2017.
- Hualei Shen, Dacheng Tao, and Dianfu Ma. Multiview locally linear embedding for effective medical image retrieval. *PLOS ONE*, 8(12):1–21, 2013.
- Ting Shu, Bob Zhang, and Yuan Yan Tang. Multi-view classification via a fast and effective multi-view nearest-subspace classifier. *IEEE Access*, 7:49669–49679, 2019.
- Tim Stuart, Andrew Butler, Paul Hoffman, Christoph Hafemeister, Efthymia Papalexli, William M 3rd Mauck, Yuhan Hao, Marlon Stoekius, Peter Smibert and Rahul Satija. Comprehensive Integration of Single-Cell Data. *Cell*, 177: (7):1888–1902, 2019.
- Tim Stuart and Ari Srivastava. Joint RNA and ATAC analysis: 10x multiomic. [https://satijalab.org/signac/articles/pbmc\\_multiomic.html](https://satijalab.org/signac/articles/pbmc_multiomic.html), 2021, Accessed: 2021-04-28.
- Jiangwen Sun, Jin Lu, Tingyang Xu, and Jinbo Bi. Multi-view sparse co-clustering via proximal alternating linearized minimization. volume 37 of *Proceedings of Machine Learning Research*, pages 757–766, 2015.
- Shiliang Sun. A survey of multi-view machine learning. *Neural Computing and Applications*, 23:2031 – 2038, 2013.
- Joshua B. Tenenbaum, Vin de Silva, and John C. Langford. A global geometric framework for nonlinear dimensionality reduction. *Science*, 290:2319–2323, 2000.
- Laurens van der Maaten and Geoffrey Hinton. Visualising data using t-sne. *Journal of Machine Learning Research*, 9: 2579–2605, 2008.
- Laurens van der Maaten and Geoffrey Hinton. Visualizing non-metric similarities in multiple maps. *Machine Learning*, 87(1), 2012.
- Nguyen Xuan Vinh, Julien Epps, and James Bailey. Information theoretic measures for clusterings comparison: Variants, properties, normalization and correction for chance. *Journal of Machine Learning Research*, 11:2837–2854, 2010.
- Bo Wang, Aziz M. Mezlini, Feyyaz Demir, Marc Fiume, Zhuowen Tu, Michael Brudno, Benjamin Haibe-Kains, and Anna Goldenberg. Similarity network fusion for aggregating data types on a genomic scale. *Nature Methods*, 11(3): 333–337, 2014.
- Minjie Wang and Allen I. Genevera. Integrative Generalized Convex Clustering Optimization and Feature Selection for Mixed Multi-View Data. *Journal of Machine Learning Research*, 22(55):1–73, 2021.
- Shiming Xiang, Feiping Nie, Chunhong Pan, and Changshui Zhang. Regression reformulations of lle and ltsa with locally linear transformation. *IEEE Transactions on Systems, Man, and Cybernetics, Part B (Cybernetics)*, 41(5): 1250–1262, 2011.
- Bo Xie, Yang Mu, Dacheng Tao, and Kaiqi Huang. m-sne: multiview stochastic neighbor embedding. *IEEE Transactions on Systems, Man, and Cybernetics, Part B: Cybernetics*, 41:1088–1096, 2011.

- Chang Xu, Dacheng Tao, and Chao Xu. A survey on multi-view learning. *ArXiv*, abs/1304.5634, 2013.
- Chang Xu, Dacheng Tao, and Chao Xu. Multi-view intact space learning. *IEEE Transactions on Pattern Analysis and Machine Intelligence*, 37(12):2531–2544, 2015.
- Dongkuan Xu and Yingjie Tian. A Comprehensive Survey of Clustering Algorithms. *Annals of Data Science*, 2(2): 165–193, 2015.
- Fanghua Ye, Zitai Chen, Hui Qian, Rui Li, Chuan Chen, and Zibin Zheng. New approaches in multi-view clustering. In *Recent Applications in Data Clustering*, chapter 11. 2018.
- Hong Yu, Xianchao Zhang, Yuansheng Yang, Xiaowei Zhao, and Lei Cai. An extended isomap by enhancing similarity for clustering. In *Advanced Research in Applied Artificial Intelligence*, pages 808–815, 2012.
- Zhenyue Zhang and Hongyuan Zha. Principal manifolds and nonlinear dimensionality reduction via tangent space alignment. *SIAM Journal on Scientific Computing*, 8:406–424, 2004.
- Jing Zhao, Xijiong Xie, Xin Xu, and Shiliang Sun. Multi-view learning overview: Recent progress and new challenges. *Information Fusion*, 38:43 – 54, 2017.
- Yue Zhao, Xinge You, Shujian Yu, Chang Xu, Wei Yuan, Xiao-Yuan Jing, Taiping Zhang, and Dacheng Tao. Multi-view manifold learning with locality alignment. *Pattern Recognition*, 78:154 – 166, 2018.
- Nanning Zheng and Jianru Xue. *Manifold Learning*, pages 87–119. 2009.
- Ying Zhu. Measuring effective data visualization. In *Advances in Visual Computing*, pages 652–661, 2007.

## A Algorithms

**Data:**  $M$  data sets,  $X_m \in \mathbb{R}^{N \times p_m}$ ,  $\forall m \in \{1, \dots, M\}$   
**Parameters:**  $Perp$  [Perplexity];  $T$  [Number of iterations];  $\eta$  [Learning rate];  $\alpha(t)$  [Momentum]  
**Result:** Induced embedding,  $Y \in \mathbb{R}^{n \times d}$ . Often,  $d = 2$   
**begin**  
  Compute pairwise affinities  $p_{i|j}^m$  with perplexity  $Perp$ ,  $\forall m \in \{1, \dots, M\}$   
  Set  $p_{ij}^m = \frac{p_{i|j}^m + p_{j|i}^m}{2n}$ ,  $\forall m \in \{1, \dots, M\}$   
  Initialise solution  $Y^{(0)} \sim \mathcal{N}(0, 0.1)$   
  **for**  $t=1$  **to**  $T$  **do**  
    Compute induced affinities  $q_{i|j}$  and set sum of gradients,  $G = 0$   
    **for**  $m=1$  **to**  $M$  **do**  
      Compute gradient  $\frac{\delta C_m}{\delta Y}$   
       $G \leftarrow G + \frac{\delta C_m}{\delta Y}$   
    **end**  
    Set  $Y^{(t)} = Y^{(t-1)} + \eta G + \alpha(t)(Y^{(t-1)} - Y^{(t-2)})$   
  **end**  
**end**

**Algorithm 1:** Multi-SNE

**Data:**  $M$  data sets,  $X_m \in \mathbb{R}^{N \times p_m}$ ,  $\forall m \in \{1, \dots, M\}$   
**Parameters:**  $k$  [Number of neighbours]  
**Result:** Induced embedding,  $\hat{Y} \in \mathbb{R}^{n \times d}$ . Often,  $d = 2$   
**begin**  
  **for**  $m=1$  **to**  $M$  **do**  
    Find  $k$  nearest neighbours of  $X^m$ .  
    Compute  $W^m$  by minimising equation (2).  
  **end**  
  Let  $\hat{W} = \sum_m \alpha^m W^m$ , where  $\sum_m \alpha^m = 1$ .  
  Compute the  $d$ -dimensional embeddings  $\hat{Y}$  by minimising equation (3) under  $\hat{W}$ .  
**end**

**Algorithm 2:** multi-LLE

**Data:**  $M$  data sets,  $X_m \in \mathbb{R}^{N \times p_m}$ ,  $\forall m \in \{1, \dots, M\}$   
**Parameters:**  $k$  [Number of neighbours]  
**Result:** Induced embedding,  $\hat{Y} \in \mathbb{R}^{n \times d}$ . Often,  $d = 2$   
**begin**  
  **for**  $m=1$  **to**  $M$  **do**  
    Construct a  $N \times N$  neighborhood graph,  $G_m \sim (V, E_m)$  with samples represented by nodes.  
    The edge length between  $k$  nearest neighbours of each node is measured by Euclidean distance.  
  **end**  
  Measure the average edge length between all nodes.  
  Combine all neighborhood graphs into a single graph,  $\tilde{G}$ .  
  In  $D_G \in \mathbb{R}^{|V| \times |V|}$ , the computed shortest path distances between nodes in  $\tilde{G}$  are stored.  
  Compute the  $d$ -dimensional embeddings  $Y$  by computing  $y_i = \sqrt{\lambda_p} u_p^i$ , where  $\lambda_p$  is the  $p^{th}$  eigenvalue in decreasing order of the the matrix  $D_G$  and  $u_p^i$  the  $i^{th}$  component of  $p^{th}$  eigenvector.  
**end**

**Algorithm 3:** multi-ISOMAP

## B Data Clustering Evaluation Measures

Let  $\mathbf{X} = \{X_1, \dots, X_r\}$  be the true classes of the data and  $\mathbf{Y} = \{Y_1, \dots, Y_s\}$  the clusterings found on  $N$  objects. In this study, we assume to know the number of clusters and thus set  $r = s$ . Let  $n_{ij}$  be the number of objects in  $X_i$  and  $Y_j$ . A contingency table is defined as shown in Table 4.

	$Y_1$	$Y_2$	$\dots$	$Y_s$	$\sum_j^s Y_j$
$X_1$	$n_{11}$	$n_{12}$	$\dots$	$n_{1s}$	$\sum_i^r n_{1i} = a_1$
$X_2$	$n_{21}$	$n_{22}$	$\dots$	$n_{2s}$	$a_2$
$\vdots$	$\vdots$	$\ddots$	$\vdots$	$\vdots$	$\vdots$
$X_r$	$n_{r1}$	$n_{r2}$	$\dots$	$n_{rs}$	$a_r$
	$\sum_i^r n_{i1} = b_1$	$b_2$	$\dots$	$b_s$	$\mathbf{S} = \sum_i^r \sum_j^s n_{ij}$

Table 4: A contingency table for data clustering.  $X_i$  refers to the  $i^{th}$  class (truth) and  $Y_j$  refers to the  $j^{th}$  cluster.  $n_{ij}$  are the number of samples found in class  $i$  and cluster  $j$ . In this study,  $r = s$  was taken, as  $K$ -means with the true number of classes known was performed.

The formulas of the four measures used to evaluate data clustering are given as follows, some with reference to Table 4.

### Accuracy (ACC)

$$(Acc) = \frac{\sum_i \sum_j \mathbb{1}\{i = j\} n_{ij}}{\mathbf{S}}$$

### Normalised Mutual Information (NMI)

$$(NMI) = \frac{2I(\mathbf{X}, \mathbf{Y})}{H(\mathbf{X}) + H(\mathbf{Y})}$$

, where  $I(\mathbf{X}, \mathbf{Y})$  is the mutual information between  $\mathbf{X}$  and  $\mathbf{Y}$ , and  $H(\mathbf{X})$  is the entropy of  $\mathbf{X}$ .

### Rand Index (RI)

$$(RI) = \frac{\binom{N}{2} - \left[ \frac{1}{2} \sum_i (\sum_j n_{ij})^2 + \sum_j (\sum_i n_{ij})^2 - \sum_i \sum_j n_{ij}^2 \right]}{\binom{N}{2}}$$

$$= \frac{\alpha + \beta}{\binom{N}{2}}$$

, where  $\alpha$  refers to the number of elements that are in the same subset in  $X$  and in the same subset in  $Y$ , while  $\beta$  is the number of elements that are in different subsets in  $X$  and in different subsets in  $Y$ .

### Adjusted Rand Index (ARI)

$$(ARI) = \frac{\sum_i \sum_j \binom{n_{ij}}{2} - \frac{\sum_i \binom{a_i}{2} \sum_j \binom{b_j}{2}}{\binom{N}{2}}}{\frac{1}{2} \left[ \sum_i \binom{a_i}{2} + \sum_j \binom{b_j}{2} \right] - \frac{\sum_i \binom{a_i}{2} \sum_j \binom{b_j}{2}}{\binom{N}{2}}}$$

## C Single-cell data

In the multi-omics single-cell data analysis, we used the publicly available data set provided by 10x Genomics for human peripheral blood mononuclear cells (PBMC)<sup>6</sup>. This data set can be downloaded and installed via the R package `SeuratData`, by running the command `InstallData("pbmcMultiome")`. In their vignette, Hoffman et al. [2021(@)] and Stuart and Srivastava [2021(@)] explored this data set to demonstrate how to jointly integrate and analyse such data.

In this data set, scRNA-seq and scATAC-seq profiles were simultaneously collected in the same cells by 10x Genomics. Data on 11909 single cells are available on 36601 genes and 108377 peaks in scRNA-seq and scATAC-seq, respectively. Cells with zero summed expression, along all genes were removed, leaving us with 10412 cells. Pre-processing was employed via the `Seurat` package, following the steps performed by Hoffman et al. [2021(@)]. Firstly, we log-normalised both data-views and then selected features for each individual data-view. In feature selection, we aim to identify a subset of features with high variability across cells (using the functions `FindVariableFeatures` and `FindTopFeatures`) [Stuart et al., 2019].

The multi-omics single-cell data set consists of 19 imbalanced clusters that correspond to their corresponding cell types; we assume the annotations provided by `Seurat` to be accurate (Figure 11). To evaluate the clustering performance of multi-SNE, we took a balanced subset of the data. Cell-type clusters with less than 200 cells were removed entirely and we combined cells with cell types under the same hierarchy. For example, *Intermediate B*, *Naive B* and *Memory B* were combined to create a single cluster, *B cells*. Similarly, *CD4 Naive*, *CD4 TCM* and *CD4 TEM* were combined as *CD4 cells*. After this process, we ended up with a subset of 9105 single cells separated in 6 cell-type clusters (*B cell*, *CD14 Mono*, *CD4*, *CD8 Naive*, *CD8 TEM* and *NK*).

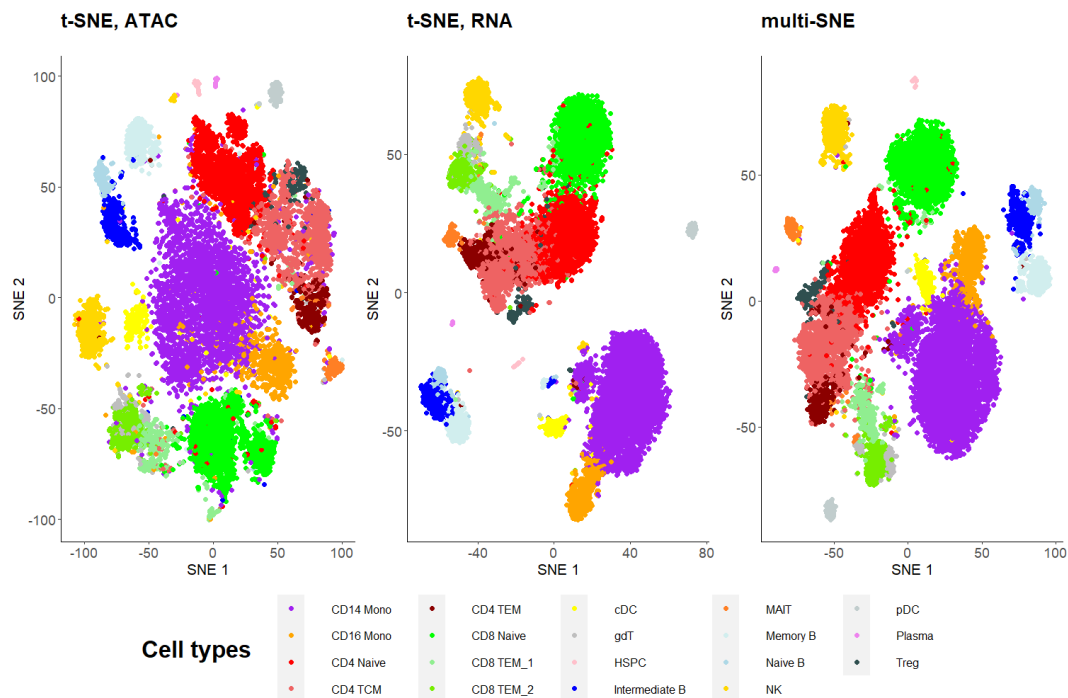


Figure 11: **Visualisations of single-cell data.** Projections of the full data set with unbalanced clusters produced by t-SNE on RNA, ATAC and multi-SNE on both data-views with perplexity  $Perp = 80$  for the two t-SNE projections and  $Perp = 20$  for multi-SNE.

<sup>6</sup> [https://support.10xgenomics.com/single-cell-multiome-atac-gex/datasets/1.0.0/pbmc\\_granulocyte\\_sorted\\_10k](https://support.10xgenomics.com/single-cell-multiome-atac-gex/datasets/1.0.0/pbmc_granulocyte_sorted_10k)

## D Additional results

### D.1 t-SNE on single-view cancer types

	ACC	NMI	RI	Adj RI
Genomics	<b>0.595</b> (0.044)	<b>0.299</b> (0.041)	<b>0.667</b> (0.017)	<b>0.253</b> (0.039)
Epigenomics	0.500 (0.036)	0.116 (0.033)	0.598 (0.018)	0.107 (0.035)
Transcriptomics	0.456 (0.023)	0.042 (0.011)	0.572 (0.006)	0.049 (0.013)

Table 5: Clustering performance on the induced embedding of a single view obtained by implementing t-SNE on Cancer Types data. Standard deviation is reported in the parentheses.

Table 5 presents the clustering performance of t-SNE applied on the three views in the cancer types data set, separately. Genomics was the favoured view on all evaluation measures.

### D.2 Handwritten digits projection in 3 dimensions (3D)

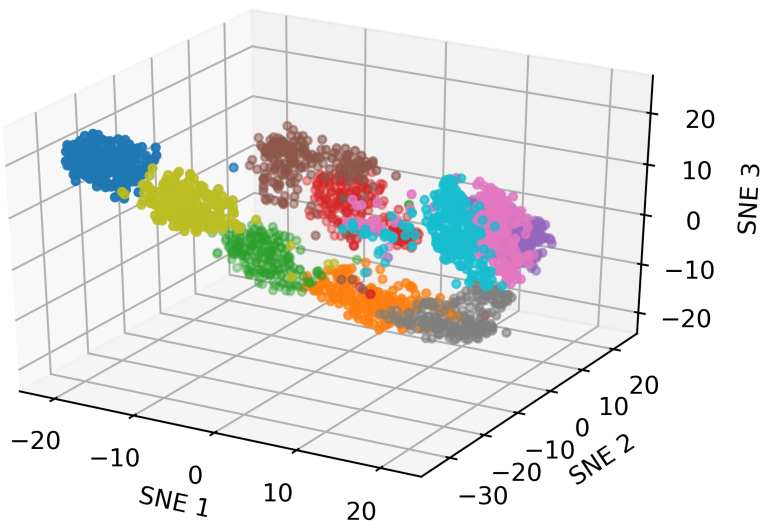


Figure 12: **3D multi-SNE visualisation of handwritten digits**. Projections produced by multi-SNE with perplexity  $Perp = 80$ . Colours present the true clustering on the data points.

## E Reproducibility

The code of multi-SNE was based on the publicly available software, written by the author of t-SNE, found in the following link:

<https://lvdmaaten.github.io/tsne/>

We refer the readers to follow the code and functions provided in the link below to reproduce the findings of this paper. The software for m-SNE and m-LLE were not found publicly available and thus we used our own implementation of the method that can be found in the same link below:

[https://github.com/theorod93/multiView\\_manifoldLearning](https://github.com/theorod93/multiView_manifoldLearning)

An R package that contains the code for multi-SNE can be installed via devtools and it can be found in <https://github.com/theorod93/multiSNE>

We refer the readers to follow the links provided in the main body of the paper for the public multi-view data used in this paper.

## F Computation time

In terms of computational time, none of the multi-view manifold learning algorithms was consistently faster than the rest (Table 6). However, multi-SNE was often the slowest algorithm, while m-SNE and multi-ISOMAP had the fastest computational time.

<b>Running time</b>	MMDS	NDS	MCS	Caltech7	Handwritten Digits	Cancer Types
m-SNE	0.43 (0.019)	0.29 (0.07)	0.42 (0.01)	4.29 (0.54)	13.34 (3.43)	251.71 (15.68)
multi-SNE	1.07 (0.100)	0.78 (0.14)	1.02 (0.01)	15.95 (0.71)	45.76 (8.44)	252.00 (11.23)
m-LLE	0.25 (0.071)	0.40 (0.12)	0.42 (0.34)	37.5 (2.21)	26.28 (8.82)	159.52 (17.49)
multi-LLE	0.28 (0.099)	0.41 (0.15)	0.30 (0.14)	37.9 (2.57)	27.94 (5.29)	157.73 (18.19)
m-ISOMAP	0.22 (0.015)	0.57 (0.06)	0.37 (0.01)	38.07 (3.09)	29.52 (5.37)	154.83 (18.04)
multi-ISOMAP	0.24 (0.032)	0.54 (0.13)	0.33 (0.05)	21.23 (2.24)	16.77 (4.65)	85.47 (14.57)

Table 6: **Averaged running time recorded in minutes.** Taken for each manifold learning algorithm on all data sets seen in this paper; standard deviation is given in the parentheses. All algorithms ran on High Performance Computing with 4 nodes.